

UNIVERSITY OF MINNESOTA

This is to certify that I have examined this copy of a master's thesis by

Roger Allen Bannister

and have found that it is complete and satisfactory in all respects,  
and that any and all revisions required by the final  
examining committee have been made.

---

Dr. Vicki L. Hansen

---

Date

GRADUATE SCHOOL

GEOLOGIC ANALYSIS OF DEFORMATION IN THE INTERIOR OF ARTEMIS  
(VENUS, 34°S, 132°E)

A THESIS  
SUBMITTED TO THE FACULTY OF THE GRADUATE SCHOOL  
OF THE UNIVERSITY OF MINNESOTA  
BY

ROGER ALLEN BANNISTER

IN PARTIAL FULFILLMENT OF THE REQUIREMENTS  
FOR THE DEGREE OF  
MASTER OF SCIENCE

MAY 2006



## **Acknowledgements**

First and foremost I would like to thank my tireless advisor, Vicki Hansen, for the countless hours spent molding my scientific mind, for her scrupulous honesty in science, and for her constant encouragement, even when it came in the form of a bleeding manuscript review. Thanks to my committee members, John Goodge and Scott Freundschuh, for their useful discussions and interesting classes. Thanks also to lab-mates Nick Lang, Kelly McDaniel, Taylor Nordberg, and Adam Brewer for hours of fruitful discussions and/or endless distractions. Last but not least, thanks to my fellow UMD geology grad students, especially roommates Isla Castañeda and Margretta Meyer, for all the good times during my stay in the twin ports, from beers at the Brewhouse to burgers at the Anchor.

## **Dedication**

To my family, Richard, Sharon, Alan, and Lisa. None of this would have been possible without your love and support.

## Abstract

Artemis, an ~2600 km diameter circular feature on Venus, is the largest known circular structure on a terrestrial planet. Artemis' most distinctive feature is Artemis Chasma, a ~25-200 km wide, ~1-2 km deep, ~2100 km diameter circular trough surrounding an interior topographic high. Artemis defies geomorphic classification. Artemis dwarfs Venus' largest impact crater, 270 km diameter Mead. Although topographically Artemis resembles some coronae, Artemis is an order of magnitude larger than the average corona and is more than twice the size of the next largest corona, Heng-O. Artemis' resembles volcanic rises and crustal plateaus in planform, yet differs greatly in topography. Detailed geologic mapping of the interior of Artemis reveals a regionally extensive penetrative tectonic fabric with a generally consistent northeast trend and average wavelength of  $\sim 520 \pm 125$  m. The interior records spatially and temporally overlapping development of four centers of tectonomagmatic activity, which each formed broadly contemporaneously with Artemis Chasma. According to four published hypotheses, Artemis represents: 1) a zone of northwest directed convergence and subduction; 2) a composite structure with the interior marking the exposure of ductily deformed deep crustal rocks analogous to a metamorphic core complex; 3) the surface expression of a bolide impact; or 4) the surface expression of a mantle plume. None of the hypotheses address the penetrative fabric. The plume hypothesis is favored as the most consistent with geologic observations; however, it requires modification to explain the penetrative fabric.

## Table of Contents

Introduction.....	1
Background.....	3
Venus .....	3
NASA Magellan Mission.....	4
Artemis Chasma and Artemis Corona .....	4
Previous Work .....	5
Data.....	9
Magellan Datasets.....	9
Obtaining Data.....	10
Methods.....	12
Interpreting Radar Imagery.....	12
Visualization Techniques.....	12
Mapping Equipment and Cartography.....	14
Mapping Criteria.....	15
Observations .....	18
Description of map units.....	18
Artemis Chasma and Exterior Deformation .....	21
Tectonomagmatic Centers .....	22
Penetrative Fabric .....	24
Implications of the Penetrative Fabric .....	28
Structure Review.....	28

Rheological ‘Thought Experiments’ .....	29
From Thought Experiments to Reality .....	32
Geologic history .....	36
Evaluation of hypotheses .....	40
Subduction hypothesis .....	40
Metamorphic core complex hypothesis .....	43
Bolide impact hypothesis .....	44
Plume hypothesis .....	46
Conclusions .....	49
References .....	50
Tables .....	55
Figures .....	58
Plates .....	see attached CD



## Introduction

Artemis is the largest circular structure (2600 km) on any of the terrestrial planets. Artemis, located in the Aphrodite Terra region of Venus (34°S, 132°E), resides between rugged highlands to the north and relatively smooth lowlands to the south (Figure 1). Artemis Chasma, Artemis' most distinctive feature, forms a ~25-200 km wide, ~1-2 km deep, and ~2100 km diameter circular trough surrounding an interior topographic high. The enigmatic nature of Artemis Chasma has perplexed researchers since it was first identified in *Pioneer Venus* data. Venus' surface abounds with circular to quasi-circular features at a variety of scales including, from smallest to largest, small shield edifices, large volcanic edifices, impact craters, coronae, volcanic rises and crustal plateaus. However, Artemis defies classification into any of these groups. Artemis dwarfs Venus' largest impact crater, 270 km diameter Mead, as well as the smaller volcanic edifices, and it lacks the basin topography, multiple ring structures, and central peak expected for large impact craters. Topographically Artemis resembles some coronae, however Artemis is an order of magnitude larger than the average corona and is more than twice the size of the next largest corona, Heng-O. In map view, Artemis' size and shape resemble crustal plateaus and volcanic rises. Volcanic rises describe broad domical regions while crustal plateaus describe steep-sided regions with flat tops; both differ greatly from the distinctive trough surrounding an interior high representative of Artemis topography.

Debate during the past decade resulted in the proposal of four hypotheses for Artemis' formation. According to these hypotheses, Artemis represents: H1) a zone of northwest-directed convergence and subduction (McKenzie et al., 1992; Brown and

Grimm, 1995; Schubert and Sandwell, 1995; Brown and Grimm, 1996); H2) a composite structure with the interior marking the exposure of ductilely-deformed deep-crustal rocks analogous to a terrestrial metamorphic core complex (Spencer, 2001); H3) the surface expression of a huge bolide impact event (Hamilton, 2005); or H4) the surface expression of a deep mantle plume (Griffiths and Campbell, 1991; Smrekar and Stofan, 1997; Hansen, 2002; Ivanov and Head, 2003). Each hypothesis makes specific predictions for deformation in the interior region of Artemis. I evaluate these hypotheses based on detailed geologic mapping of Artemis' interior using NASA *Magellan* synthetic aperture radar (SAR) imagery and topography data.

## **Background**

### *Venus*

Venus, commonly referred to as Earth's sister planet, nearly equals the Earth in size, bulk density, and distance from the Sun (Table 1) suggesting that the bulk composition and heat budget of Venus should be broadly similar to the Earth (e.g., Grimm and Hess, 1997). Despite these similarities, Earth and Venus evolved quite differently, resulting in a diversity of surface deformation styles. Conditions at the Venusian surface are inhospitable to humans, with a temperature of  $\sim 762$  K ( $\sim 482^\circ$  C), a caustic, dominantly CO<sub>2</sub> atmosphere at a pressure of  $\sim 92$  bars, and only trace amounts of water. The Earth's crust differentiated into granitic continental crust and basaltic oceanic crust, reflected in the bimodal distribution of the hypsometric curve for the Earth. Limited geochemical evidence from a series of Soviet *Venera* lander missions indicates a Venusian crustal composition that resembles basalt (Barsukov et al., 1982; Surkov et al., 1987). The hypsometric curve for Venus displays a unimodal distribution implying the crust is not differentiated in the same manner as the Earth (Rosenblatt et al., 1994). Terrestrial plate tectonic processes — manifested in curvilinear features such as orogenic belts, subduction zones, oceanic spreading centers, and transform fault zones — provides a mechanism for interior heat to travel to the surface on Earth. Venus lacks such globally pervasive curvilinear features and instead circular features dominate the surface, suggesting that Venus loses its heat in a different manner (e.g., Solomon et al., 1991; Phillips and Hansen, 1994)

### ***NASA Magellan Mission***

The NASA *Magellan* mission to Venus was launched in 1989 to obtain near global radar images of Venus at a resolution better than 300 m and a near global topographic map with horizontal resolution of ~10 km and vertical accuracy of 80 m or better (Saunders et al., 1992; Ford et al., 1993). *Magellan* collected correlated synthetic aperture radar (SAR) images, emissivity, root-mean-square (RMS)-slope, reflectivity, and altimetry data across three mapping cycles and gravity data across two cycles. This wealth of data provides the opportunity to better understand the geologic characteristics of Venus. The *Magellan* datasets as they apply to this research are discussed further in the data section of this text.

### ***Artemis Chasma and Artemis Corona***

Artemis Chasma, named for the Greek goddess of the hunt, was first identified in low-resolution radar data from the NASA *Pioneer Venus Orbiter* mission. Stofan et al. (1992) categorized Artemis as a corona after *Magellan* data became available, although it is unclear if Artemis is still included in Stofan's corona database. The term corona (from the Latin word meaning "crown," plural coronae) originated as a descriptive term covering any quasi-circular structure defined primarily by an annulus of concentric fractures and/or ridges. The term gained genetic connotations as the body of corona research grew. Most researchers favor diapiric mechanisms for the formation of coronae (Squyres et al., 1992; Stofan et al., 1992; Koch and Manga, 1996; Smrekar and Stofan, 1997; Stofan et al., 1997). However, the diversity of morphologies and range of sizes indicate that coronae may form by a variety of processes including caldera collapse

(Squyres et al., 1992) and bolide impacts (Hamilton, 2005; McDaniel, 2005; McDaniel and Hansen, 2005; Vita-Finzi et al., 2005). Although Stofan et al. (1992; 1997) suggested that the various morphologies of coronae represent different stages of corona development, coronae display no obvious age progression where they occur in chains or clusters (Hamilton and Stofan, 1996; Stofan et al., 1997). Artemis dwarfs the mean corona size (~200 km diameter) by an order of magnitude and is over twice the size of the next largest corona, ~1000 km diameter Heng-O. This vast size difference raises concern over classifying Artemis as a corona.

This paper follows the terminology of Hansen (2002), where the term Artemis refers to the entire large circular geomorphic feature centered at 33°S, 133°E, including Artemis Chasma, the raised interior region, and the adjacent exterior region. This broad definition of Artemis helps to distance it from the genetic connotations and assumptions associated with the word corona.

### ***Previous Work***

#### ***Mapping***

Brown and Grimm (1995) constructed a geologic map of Artemis, focusing on Artemis Chasma. They compiled a geologic map at a scale of 1:3,000,000, which they published as a simplified tectonic sketch map (Figure 2). Brown and Grimm used all available NASA *Magellan* cycle 1, 2, and 3 SAR images at F, C1, and C2 scales, as well as GTDR topography data (see Data section of this text for an explanation of NASA *Magellan* products), although their visualization techniques differ from those used here. They used the so-called “magic-airbrush” technique (Kirk, 1993) to create shaded-relief

images, which operates on the premise that the surface roughness and dielectric constant contributions to radar signal strength should be similar between left- and right-look images, whereas the slope effects should be quite different. By calculating a weighted difference between left- and right-look images, effectively removing the roughness and dielectric constant components, only the slope component of image brightness remains. While this method produces shaded-relief images at the resolution of the SAR imagery used, it is important to note that this method preserves radar foreshortening and elongation effects (discussed in detail in the Methods section of this text) which can complicate interpretation of the cross-sectional shape of topographic features.

Hansen's (2002) geologic map focuses on Artemis' interior, chasma, and exterior regions, although in less detail than presented here. Hansen used all available NASA *Magellan* SAR image data (F-, C1-, and C2-scale, cycles 1, 2, and 3) and topography data. Inverted SAR images were used to highlight structural lineaments, and synthetic stereo imagery (Kirk et al., 1992) was used to visualize data in three dimensions, combining SAR and topographic relations. Hansen published a reduced version of a geologic map of Artemis compiled at a scale of 1:5,000,000 (Figure 3). The geologic maps of Hansen (2002) and Brown and Grimm (1995) broadly agree in the location and characterization of structural features. Hansen's (2002) map covers a slightly larger region and is more detailed both in structures and the consideration of geologic units, as expected for a later work.

Spencer (2001) examined deformation in the center of Artemis at a low level of detail. Spencer published a sketch map of the "central interior deformation belt" (Figure

4); the sketch map lacks many significant structures in the area, most notably the fine-scale fabric of Figure 2 and the penetrative fabric of Figure 3.

### Modeling

Brown and Grimm (1996) followed their tectonic analysis of Artemis Chasma with flexural modeling of the outer rise near the southeast portion of Artemis Chasma. Their inelastic and elastic flexural modeling, aimed at estimating local geothermal gradients and lithospheric rheology, hinged on the assumption that Artemis Chasma is analogous to terrestrial subduction zones as proposed by various authors (Sandwell and Schubert, 1992; Brown and Grimm, 1995; Schubert and Sandwell, 1995). Importantly, this modeling focused on the southeast portion of Artemis Chasma because that is where the chasma trends perpendicular to a proposed northeast direction of convergence.

Griffiths and Campbell (1991) conducted lab experiments aimed at modeling the interaction of large thermal mantle plumes with the lithosphere. As a plume head approaches a rigid boundary it flattens and spreads laterally. As mantle is squeezed out from between the plume head and the rigid layer (lithosphere), a ring-shaped instability develops, forming an axisymmetric trough. These workers noted the similarity of this trough, which formed in experiments, and the trough of Artemis Chasma. These experiments provided the foundation for a plume hypothesis for Artemis' formation. Finite-element modeling of the interaction of a large thermal mantle plume with the lithosphere aimed at modeling corona topography also shows the development of an axisymmetric trough (Smrekar and Stofan, 1997).

## Gravity

Schubert et al. (1994) conducted a gravity data analysis of coronae and chasmata on Venus. A semi-circular positive gravity anomaly of 20-40 mgal lies along Artemis Chasma (Figure 5), most prominently expressed at the southeast portion of the interior. Schubert et al. (1994) calculated a best-fit apparent depth of compensation (ADC) of  $200 \pm 12.5$  km for the large gravity anomaly and about  $50 \pm 12.5$  km for the Artemis region in general, a gravity/topography ratio of  $0.056 \pm 0.008$  mgal/m, and a geoid/topography ratio of  $35 \pm 5$  m/km for the Artemis region. Gravity analyses provide some insight into subsurface structure, however interpretations of lithosphere structure based on gravity are inherently non-unique. For instance, the gravity/topography data for Artemis is consistent with partial dynamic support, very thick lithosphere ( $>100$  km), or a combination thereof (Schubert et al., 1994; Simons et al., 1997).



## Data

### *Magellan Datasets*

The NASA *Magellan* mission (1991-1994) produced an amazing digital correlated geophysical data set for Venus with near global (~98%) coverage (Saunders et al., 1992; Ford et al., 1993). The *Magellan* radar sensor acquired data in three modes; synthetic aperture radar (SAR), radiometer, and altimeter mode. The system used a 3.7 m diameter parabolic high-gain antenna (HGA) fixed 25° off nadir perpendicular to the trajectory of the spacecraft in SAR and radiometer modes. The SAR operated with a 12.6 cm wavelength at 2.385 GHz (S-band) with horizontal parallel transmit/receive polarization (HH) in order to penetrate the thick, CO<sub>2</sub>-dominated cloud cover. SAR images were produced in 3 cycles with varying look geometries (left-looking, right-looking, and stereo left-looking) to cover ~98% of the planet surface. The altimeter mode used a smaller altimeter horn antenna (ALTA) fixed in the nadir direction. Figure 6 illustrates the geometry of *Magellan* observations. Table 2 summarizes the radar and orbital characteristics. Due to the elliptical orbit the SAR incidence angle was varied with latitude to provide an optimum signal to noise ratio. In the Artemis region incidence angles range from ~38-23°, ~25°, and ~20-14° from north to south for cycles 1, 2, and 3 respectively. SAR image resolution is approximately 100 m.

The size of the altimeter footprint varies with spacecraft altitude and therefore varies with latitude. In the Artemis region footprints measure 8-11 km in along-track dimension and 19-24 km in cross track dimension (Ford et al., 1993). Combining the surface-to-spacecraft distance with the known position of the spacecraft relative to the

planetary center produces a global topographic data record (GTDR) with horizontal resolution ~10 km and vertical resolution ~80 m. Reflectivity and RMS-slope data sets were also derived from the altimetry data. Emissivity data were derived from radiometry measurements interleaved with the SAR observations. Gravity data were collected during cycles 4 and 5 before the spacecraft was intentionally crashed in an effort to circularize the orbit to increase gravity data resolution in the polar regions.

This study primarily uses SAR image mosaics from cycles 1, 2, and 3, including both left-looking and right-looking images (Figure 7). Compressed once (C1-MIDR) and compressed twice (C2-MIDR) SAR images are used for regional analysis while full resolution images (F-MIDR) are used for detailed analysis of areas of interest (resolution of SAR images are ~225, ~675, and ~75 m/pixel respectively). GTDR data is used for analysis of regional topography and to assist in visualization in three dimensions.

### ***Obtaining Data***

Data for this study were provided by the USGS Astrogeology Team in the projection parameters for the Artemis Chasma (V-48) quadrangle (Lambert conformal conic, standard parallels at 34° S and 73° S, central meridian 135°E, latitude of origin 90° S). Left-look (cycle 1) F-MIDR (~75 m/pixel), left-, right-, and stereo-look (cycles 1-3) C1-MIDR (~225 m/pixel) SAR imagery were provided in TIFF and BIL formats. Topography, emissivity, RMS-slope, and reflectivity data were provided in TIFF, BSQ, and ASCII formats. All *Magellan* data used in this study are also available online from the USGS Map-a-planet website (<http://pdsmaps.wr.usgs.gov/>) and the USGS Planetary

GIS Web Server (PIGWAD, <http://webgis.wr.usgs.gov/>) in a variety of formats, although not in the projection parameters for the V-48 quadrangle.

## **Methods**

### ***Interpreting Radar Imagery***

Radar image brightness is a function of the roughness, topography, and electrical properties of the imaged surface. Basically, surfaces that are inclined towards the incident radar and/or are rough at or above the scale of the radar wavelength (12.6 cm) appear radar-bright; surfaces that are inclined away from the incident radar and/or are smooth (below the scale of the radar wavelength) appear radar-dark (Figure 8). The opposite is true for inverted SAR images. Inverted SAR images are useful for structural analysis because structural elements (typically lineaments) tend to show up better in negative SAR images (Figure 9). Due to the geometry of radar imagery, echoes off areas of high elevation return to the antenna before echos from areas of low elevation. This causes mountain peaks to image forward of their actual position, known as ‘foreshortening’; the opposite occurs on the back slope, known as ‘elongation’. If the echo from the peak returns before the echo from the forward toe, then the peak will be imaged on top of the base, an effect known as ‘lay-over’. A surface inclined away from the radar look direction at an angle greater than the incidence angle will lie in radar shadow and will not be imaged. These effects complicate SAR image interpretation but once understood, SAR imagery can provide a tool for determining short-wavelength topography.

### ***Visualization Techniques***

Stereo imagery can greatly enhance the interpretation of landforms by displaying data in three dimensions. Parallax differences between two images with different viewing geometries produce a sense of depth when viewing the images with a stereoscope (or

with red-blue glasses if the images are combined to form a red-blue anaglyph). In the case of *Magellan* SAR data, image pairs with opposite look directions are difficult to visually merge because the illumination direction changes drastically between the two images; however, stereo pairs with the same look direction but different incidence angles (i.e. cycle 1 and cycle 3 left-look SAR images) can be combined to great effect. Unfortunately, cycle 3 coverage of Artemis is patchy and limited to a small portion of the northeast; therefore, true stereo coverage of Artemis is poor.

Cycle 1 left-looking SAR and cycle 2 right-looking SAR coverage of Artemis is nearly complete. Synthetic stereo pairs (Kirk et al., 1992) for each data set are created by introducing distortion to an image based on the GTDR for the same area using the displace filter in Adobe Photoshop<sup>®</sup>. Combining the images by placing the original image on the red channel and the distorted image on the blue and green channels produces a red-blue anaglyph that can be viewed with red-blue glasses, thus allowing direct spatial correlation of SAR imagery with topography data. Regional topographic trends are easily gleaned from synthetic stereo images. Synthetic stereo images do not, however, resolve subtle topographic features that might be resolved in true stereo images; there is a sacrifice of image resolution in the synthetic stereo images because of the low resolution of the topography data (Figure 10). The method for creating synthetic stereo imagery may also be applied to the other geophysical data sets (emissivity, RMS-slope, reflectivity, and gravity) for enhanced three-dimensional visualization of those data sets.

Simulated three-dimensional perspective views, 3D models, and fly-by animations provide supplemental visualization of Artemis. These visualization techniques

are well-suited for illustrative purposes, however caution should be exercised when making scientific interpretations due to the vertical exaggeration (typically 20 times or more) used in creating these images.

Color overlay methods, which combine elevation data and SAR imagery were used to a limited extent in this study. Images are produced by breaking-down a color coded topography image into hue, saturation, and intensity components and substituting a SAR image for the intensity component (Ford et al., 1993). This technique allows visualization of topography without the loss of resolution in the SAR image that occurs in the synthetic stereo image process and it is compatible with the human eye's natural ability to discern intensity differences with more acuity than color differences. Additionally these images can convey topography to those who cannot successfully view stereo imagery.

### ***Mapping Equipment and Cartography***

I geologically mapped the interior of Artemis that falls within the V-48 quadrangle with north-south bounds of 25° S to 50° S and east-west bounds of 120° E to 150° E at a scale of 1:5 million. I mapped using data projected to the V-48 quadrangle parameters to facilitate the eventual submission of this map to the United States Geological Survey. Most of the interior region of Artemis (greater than ~90%) lies within this region and therefore coverage was deemed sufficient for this purpose to avoid the nontrivial task of projecting data from the neighboring quadrangles to the parameters of V-48.

Mapping was accomplished using Adobe Illustrator 10™ running on an iMac G4 with a Wacom Cintiq 15X LCD write-on tablet. MAPublisher 6.2™, a plug-in for Adobe Illustrator™, was used to scale and place each georeferenced raster dataset appropriately at the 1:5 million scale. The graticule and synthetic stereo images of the C1 SAR images were produced using a custom program and macros authored by Duncan A. Young. SAR images were stretched and inverted using Adobe Photoshop CS™. Topographic profiles and shaded relief images were generated with ArcGIS 9.1.

### ***Mapping Criteria***

Geologic mapping was conducted according to guidelines set forth by Tanaka et al. (1994) with caveats highlighted by Hansen (2000). Material units are defined by morphology, primary structures, and radar characteristics of units emplaced coherently in a discrete period of geologic time. Terrain units are defined texturally by secondary structures and indicate a shared geologic history of materials after the emplacement of secondary structures that combined potentially previously unrelated material units. Terrain units do not imply a shared history or genetic relationship prior to the deformation that emplaced their characteristic textures. Material units, terrain units, primary structures, and secondary structures all provide clues to formative processes, material properties (i.e. rheology), and geologic history (Hansen, 2000).

### **Primary Structures**

Primary structures are structures that formed during the emplacement of geologic units. Flow fronts, shield edifices, and impact craters are some examples of primary structures (Figure 11). Definitions of primary structures mapped are as follows:

*Shields:* small (<1-15 km diameter) circular to quasi-circular features with dome, cone, shield, or flat-topped shapes with or without a central pit (Guest et al., 1992), interpreted as small volcanic edifices.

*Channels:* narrow (~1 km) steep-sided, shallow (on the order of 10s of meters), sinuous troughs morphologically similar to terrestrial fluvial channels (Baker et al., 1992; Komatsu and Baker, 1994), interpreted to form by channelized fluid flow, possibly in the shallow subsurface (Lang and Hansen, 2006).

*Pit chains:* a collection of small (<1-10 km diameter) circular to elliptical pit craters arranged in a line, interpreted as the result of stoping of material during emplacement of magmatic dikes (Okubo and Martel, 1998).

*Shallow trough:* a pair of closely spaced (<5 km) lineaments marking a shallow (10s of meters) flat depression bounded by steep sides; interpreted herein as the result of subsurface magmatism.

*Flow direction:* direction of flow inferred from channels, levees, and other volcanic constructs.

*Flow front:* the typically lobate margin of a discrete lava flow.

*Radar boundary:* a sharp transition in radar brightness, too ambiguous in character to classify as a flow front; typically lobate in V-48.

*Crater rim crest:* the raised rim of an impact crater enclosing an interior basin.



## Secondary Structures

Secondary structures are structures that formed after the emplacement of geologic units. Folds, fractures, and penetrative fabric are some examples of secondary structures (Figure 12). Definitions of secondary structures mapped are as follows:

*Fracture:* lineaments with a negative, or null, topographic signature, commonly grouped into suites based on orientation, pattern (i.e. radial, concentric) and/or spacing (i.e. widely-spaced vs. closely-spaced); interpreted as extensional structures.

*Folds:* ridges with a gradational radar character across strike and wave-like topographic expression; interpreted as contractional structures.

*Small ridge:* topographic ridge with low relief and width, similar in appearance to folds except origin is ambiguous, but possibly contractional.

*Large ridge:* topographic ridge with moderate relief and width.

*Penetrative fabric:* closely spaced (0.5-1 km) lineaments with slight gradation in radar brightness across strike; interpreted in some cases as short-wavelength low-amplitude folds, in other cases as fracture-like structures, however in other cases the fabric character is ambiguous.

*Lineament:* discrete lineament with ambiguous topographic expression and undetermined origin.

## **Observations**

Geologic mapping of Artemis' interior (Plate 1, Artemis Map) reveals a rich record of deformation and volcanic activity. In this section I discuss key geologic observations from Artemis' interior that prove important to understanding Artemis' geology and the interpretation of the geologic history discussed in the following section.

### ***Description of map units***

#### **Terrain units:**

**Basal terrain a of Artemis (btaA)** – High to very high-backscatter, high RMS slope, host to dominantly northeast-southwest trending 0.3-0.6 km wavelength penetrative tectonic fabric of undetermined origin. Gradational contact with unit btbA.

*Interpretation:* Local basal material.

**Basal terrain b of Artemis (btbA)** – Moderate-backscatter, high RMS slope, host to dominantly northeast-southwest trending 0.3-0.6 km wavelength penetrative tectonic fabric of undetermined origin and topographic ridges spaced 10-50 km. Gradational contact with unit btaA. *Interpretation:* Local basal material.

**Basal fracture terrain of Zhibeck Planitia (bftZ)** – moderate to low backscatter, low regional relief, terrain exposed locally through surrounding regions, and marked by penetratively developed parallel fracture. *Interpretation:* Materials of unknown genetic origin deformed by regional and local tectonic structures prior to being locally covered.

**Shield terrain (st)** – intermediate-to-low backscatter material of heterogeneous texture. Composed of distributed edifices and associated material that forms a locally thin layer.

*Interpretation:* Composite shield-related volcanic materials.

Material units:

**Shield field and associated flow material a of Artemis (sfaA)** – Low-backscatter, low RMS slope, pock-marked by shield edifices less than 5 km in diameter, sharp digitate boundaries with kipukas of unit btaA, located in the southwest region of Artemis.

*Interpretation:* Localized thin, low-viscosity veneer of volcanic shields and associated deposits.

**Shield field and associated flow material b of Artemis (sfbA)** – Low-backscatter, low RMS slope, pock-marked by shield edifices less than 5 km in diameter, sharp digitate boundaries with kipukas of unit btaA, located in the southeast region of Artemis.

*Interpretation:* Localized thin, low-viscosity veneer of volcanic shields and associated deposits radiating from a centralized source.

**Shield field and associated flow material c of Artemis (sfcA)** – Low-backscatter, low RMS slope, pock-marked by shield edifices less than 5 km in diameter, sharp digitate boundaries with kipukas of unit btaA, located in the eastern region of Artemis.

*Interpretation:* Localized thin, low-viscosity veneer of volcanic material associated with volcanic shields.

**Flow material of Quilla Chasma (fQc)** – Low-backscatter, low to moderate RMS slope, lobate to gradational boundaries, extends into local topographic lows. *Interpretation:* Localized volcanic material sourced from structures related to Quilla Chasma (V-36).

Composite units:

**Flow material a of Artemis (fcaA)** – Low-backscatter, low RMS slope, locally pock-marked by small shield edifices (less than 5 km diameter), localized lobate flow fronts,

deformed by magmatic troughs, local inliers of unit btaA, located in the western region of Artemis. *Interpretation:* Composite of volcanic flows emplaced after the formation of the basal terrains.

**Flow material b of Artemis (fcbA)** – Very low to moderate-backscatter, low RMS slope, pock-marked by small shield edifices (less than 5 km diameter), localized lobate flow fronts, locally hosts fine-scale polygonal fabric near the eastern margin, contact with unit btaA is in general digitate where the contact is at high angles to the trend of the penetrative fabric of unit btaA and gradational where the contact is near parallel to the trend of the penetrative fabric; embays unit mAc on the eastern-southeastern margin, located in the eastern region of Artemis. *Interpretation:* Composite of volcanic flows emplaced after the formation of the basal terrains.

#### Radar units

**Radar facies (rf)** – high backscatter radar facies marked by penetratively developed (i.e., spaced at or below data resolution) tectonic fractures and flows (?). Major trends marked by lineaments. This facies does not represent a single coherent geologic unit formed at a specific time, or of a specific character. *Interpretation:* Radar facies representing a composite unit of tectonic fabrics and flows.

#### Undifferentiated materials:

**Localized flow material; undifferentiated (lfu)** – Low-backscatter, low-RMS slope material located in local topographic lows, commonly associated with small shield edifices (less than 5 km diameter). *Interpretation:* Localized flood lava flows.

**Crater fill material (cfi)** – Undifferentiated, low-backscatter, low-RMS slope material filling some impact basins. *Interpretation:* Gently emplaced material postdating impacts, possibly volcanic.

**Crater flow material (cfl)** – Undifferentiated, high-backscatter material apparently flowing from some impact basins. *Interpretation:* Impact melt or fluidized ejecta created by bolide impact.

**Crater ejecta material (ce)** – Undifferentiated, moderate to high-backscatter, high-RMS slope material. *Interpretation:* Near-field ejecta and structurally uplifted breccia associated with bolide impact.

**Crater central peak material (ccp)** – Undifferentiated, high-backscatter, high-RMS slope material located near the center of some impact basins as isolated inliers. *Interpretation:* Structurally uplifted breccia or rebounded material associated with bolide impact.

**Flow material; undifferentiated (fu)** – Undifferentiated, low to moderate-backscatter, low-RMS slope, texturally homogenous, discontinuous radar-boundaries, locally pock-marked by small shield edifices (less than 5 km in diameter), locally deformed by fractures, pit chains, and magmatic troughs. *Interpretation:* Composite of individual local to regional events, unlikely to represent a coherent stratigraphic unit across entire map area.

### ***Artemis Chasma and Exterior Deformation***

Artemis Chasma forms a well-defined circular trough that encloses approximately three quarters of Artemis interior. The chasma ranges in width from ~25 to ~300 km and

displays an average relief of ~1-2 km. Artemis Chasma fades away in the northwest and increases in width and depth to its maximum in the southeastern to eastern portion. The chasma hosts a tectonic fabric of trough-parallel folds and lineaments that increase in intensity counterclockwise from the northwest (Brown and Grimm, 1995; Hansen, 2002). Radial fractures and concentric wrinkle ridges deform the undivided flow material outward of Artemis Chasma. A full tectonic analysis of Artemis Chasma and deformation outboard from it is beyond the scope of this project; instead the reader is referred to the thorough works of Brown and Grimm (1995) and Hansen (2002).

### ***Tectonomagmatic Centers***

Artemis' interior preserves four centers of tectonic and magmatic activity defined by radial and/or concentric fractures or lineaments and discrete lava flows. Hansen (2002) described these centers as corona-like features, though in the interest of objectivity I refer to them herein as tectonomagmatic centers, labeled TMa-d (Plate 1). Each of these centers is discussed briefly below.

TMa ('C4' and 'C3' (Hansen, 2002), 'southwestern interior deformation belt' (Spencer, 2001)) is defined by radial fractures, concentric ridges, weakly concentric fractures, radial lava flows, and the low-backscatter material of unit sfbA. A shallow topographic trough wraps around from the northern margin to the western margin of TMa (most of Brown and Grimm's (1995) north-northwest-trending deformation belt). A large scarp lying on the north side of the shallow trough roughly defines the southern extent of TMa. Unit sfaA hosts numerous small shield edifices and kipukas of unit btaA. Unit sfaA interfingers with unit btaA, filling long, narrow, shallow valleys. Unit sfaA locally covers

earlier formed tectonic fabrics and is cut by northeast-trending fractures that may represent reactivation of buried structures. I interpret these relations to indicate that unit sfaA is thin (10's of meters) and had a low emplacement viscosity. Impact crater Bonnevie (diameter ~80 km) lies along the eastern margin of unit sfaA. Robustly constraining temporal relations between Bonnevie and unit sfaA proves difficult due to the degraded state of the crater ejecta. The eastern portion of TMa ('C3' (Hansen, 2002)) hosts radial fractures that weakly define a secondary center. Volcanic flows emanate from the eastern margin and extend eastward and southeastward towards TMb.

TMb ('C2' (Hansen, 2002)) is defined by radial fractures, distal concentric fractures, and the low-backscatter material of unit sfbA. Unit sfbA hosts numerous small shield edifices with one ~5 km-diameter volcanic edifice near the center. Unit sfbA contains kipukas of unit btaA and delicately interfingers with unit btaA, filling long, narrow, shallow valleys implying a low emplacement viscosity. A northwest-trending scarp forms the transition between unit btaA and fcbA, where a distinct lava flow in unit fcbA, apparently sourced near the scarp, extends approximately 200 km towards TMa. Northwest-trending fractures located northeast of unit sfbA cut a radial fracture suite. Widely-spaced (10's of km) arcuate fractures to the northeast define a circle centered approximately on unit sfbA.

TMc ('C1' (Hansen, 2002)) is defined by radial fractures tracing back to the low-backscatter material of unit sfcA. Unit sfcA hosts numerous small shield edifices and interfingers with unit btaA, filling long, narrow, shallow valleys implying a low viscosity during emplacement. Penetrative fabric trends northwest/southeast and parallels a suite of

quasi-radial fractures. Three moderately sized (10's of km) volcanic edifices lie to the north of TMc in unit btaA. The volcanic flows of composite unit fcbA fan away from TMc and locally cover the tectonic fabrics of unit btaA.

TMd ('C5' (Hansen, 2002); northeast-trending deformation belt (Brown and Grimm, 1995); northeastern interior deformation belt (Spencer, 2001)) dominantly consists of sub-parallel northeast-trending rounded ridges and lava flow-filled valleys. TMd lies predominantly in unit btbA, which grades into the adjacent unit btaA. The ridges parallel the penetrative fabric trend and preserve the penetrative fabric. Brown and Grimm (1995) identified northeast-trending flat-topped ridges which they interpreted as horsts and adjacent flat-floored valleys as graben. I do not observe flat-topped northeast-trending ridges in this area; rather I observe rounded ridges and angular peaked ridges. This discrepancy in observations between authors likely arises from angular ridges appearing as flat-topped ridges due to radar image artifacts preserved by the "magic airbrush" technique used by Brown and Grimm (1995). Northwest-trending fractures, scarps, and penetrative fabric in the northern part of TMd cut northeast-trending tectonic fabrics. Northwest-trending fractures in the southern part of TMd cut northeast-trending penetrative fabric. Roughly concentric fractures and scarps, which lie to the west of TMd also cut penetrative tectonic fabric and ridges.

### ***Penetrative Fabric***

A remarkably developed penetrative tectonic fabric occurs throughout the basal terrains of Artemis. This fabric consists of tightly-spaced lineaments that commonly form low-amplitude rounded ridges, although fracture-like topographic expressions and



ambiguous topographic expressions also occur (Figure 13). The lineaments display a generally consistent northeast trend, however locally lineaments show a perpendicular trend (Figure 14). Although local minor deviations from the northeast trend may reflect small-scale topography and/or heterogeneity in the deformed material, perpendicular trends likely require a tectonic explanation. The penetrative fabric is consistent in character along strike as well as across strike, displaying no regular gaps or correlation with parallel long-wavelength structures.

SAR imagery provides clues about the cross-sectional topographic shape of the penetrative fabric and therefore fabric morphology. The fabric appears similar in left-look and right-look SAR images (Figure 15 D and E), leading to the assumption that the fabric's cross-sectional topographic shape is approximately symmetrical. Figure 15 compares the predicted radar return of three symmetrical low-amplitude topographic shapes with the same periodicity (wavelength). The predicted radar return patterns were constructed using an incidence angle typical of left-looking SAR for the area ( $\theta=30^\circ$ ) and two reasonable simplifying assumptions: 1) the radar source is sufficiently distant that the radar signal rays are parallel, and 2) the material is isotropic with respect to radar so that change in slope is the only cause of variation in signal return. Steep-sided troughs with flat-topped ridges and flat-bottomed valleys (Figure 15 A) produce a sharply alternating pattern of high return from the radar-facing slopes and radar shadow due to the slopes facing away from the radar, punctuated by moderate to low return from the flat surfaces. A wrinkled surface with angular ridges and valleys (Figure 15 C) results in a bimodal radar image with foreshortened high-return radar-facing slopes and elongated low-return

opposite-facing slopes. Rounded ridges and valleys (Figure 15 B) produce a gradational radar image because slope constantly changes with respect to the radar incidence angle. Radar-facing slopes are foreshortened while slopes facing away from radar are elongated resulting in a compressed gradation from moderate to high return paired with an expanded gradation from moderate to low return. The penetrative fabric has a gradational character across strike in both left-looking (Figure 15 D) and right-looking SAR (Figure 15 E); low-amplitude rounded ridges best fit the observations.

Penetrative fabric wavelength is generally consistent across Artemis. Penetrative fabric wavelength was measured at 19 locations across Artemis (Table 3, Plate 1), along transects perpendicular to fabric trend. Stretching the contrast of the inverted SAR imagery enhanced the difference between light and dark lineaments. The number of dark lineaments along each transect divided into the total length of the transect yields the average wavelength at each location. Wavelength ranges from 303-952 m with an average of  $540 \pm 157$  m. Ignoring one high outlier results in a range from 303 m to 731 m with an average of  $\sim 520 \pm 125$  m. Note that these values represent a maximum wavelength because the wavelength approaches the effective resolution of the *Magellan* SAR data (e.g., Zimelman, 2001).

The penetrative fabric primarily occurs in units btaA and btbA (Plate 1), however the fabric locally extends into adjacent units. Penetrative fabric mapped outside of btaA and btbA always occurs at gradational contacts determined primarily by a gradual decrease in radar backscatter, whereas fabric-parallel lineaments remain easily identifiable but appear slightly subdued. The subdued appearance may reflect weathering,

varying degrees of burial by thin volcanic flows or aeolian fines, and/or reactivation of buried fabric structures. Low-backscatter material interfingers with the penetrative fabric in some locations (Figure 13). The delicate interfingering relationship indicates that the low-backscatter material constitutes a thin veneer requiring a low viscosity during emplacement to fill the long, narrow, and shallow valleys without completely burying the penetrative fabric. The low-backscatter materials are interpreted as local volcanic deposits. A sedimentary origin is unlikely due to the present lack of significant erosion rates and the pristine appearance of adjacent rocks that would be the most probable source of sediment. Penetrative fabric-parallel lineaments in the low-backscatter material likely represent reactivation of buried penetrative fabric structures.

## **Implications of the Penetrative Fabric**

The morphology of the penetrative fabric provides constraints for mechanisms of its formation. This section explores the constraints the presence of the penetrative fabric imposes on Artemis' geology.

### ***Structure Review***

Pressure, temperature, composition, presence of fluids, heterogeneity, and strain rate all affect the rheological behavior of materials and thus influence the style and distribution of deformation. Broadly speaking, when the effective stress on a material reaches the material's yield strength the material will respond by: 1) brittle failure, where the material breaks into two or more separate pieces, or 2) ductile failure, where the material flows plastically in a continuous fashion. The change in size and shape of a rock experienced during deformation is known as strain. Structures visible at the surface may provide information about the orientation of the bulk strain in an area. The strain ellipsoid provides a powerful tool with which to consider strain and strain history, by graphically illustrating the orientation and magnitude of the lines of maximum, minimum, and intermediate elongation. If we assume that no change in shape occurs along the intermediate axis (plane strain) we can simplify our consideration of strain to two-dimensions represented by a strain ellipse. The along-strike consistency of the penetrative fabric and lack of related perpendicular structures supports the assumption of plane strain. In the following discussion I use strain ellipses only to qualitatively illustrate the orientation of 2D-strain and do not attempt to quantify the amount of strain.

Structures come in a variety of styles and morphologies characteristic of their mode of formation (i.e. brittle or ductile). Fractures are brittle features that form sharp lineaments that may be laterally extensive. Ductile folds form by a variety of mechanisms but all display an undulating morphology consisting of periodically spaced rounded ridges and valleys. Boudins result from failure of a competent layer sandwiched between weak layers. Brittle boudins display sharp geometries whereas ductile boudins (also termed pinch and swell structures) form rounded geometries (see discussion in Price and Cosgrove, 1990).

Fracture spacing and fold wavelength are each related to the effective mechanical thickness of the deformed material (e.g. Pollard and Aydin, 1988; Price and Cosgrove, 1990 and references therein). Empirical observation, theoretical considerations, and numerical and physical modeling indicate wavelength to thickness ratios ( $\lambda/H$ ) typically range from 1-3 for extensional features (e.g. Ramberg, 1955; Price and Cosgrove, 1990) and 3-6 for folds (e.g. Biot, 1961; Sherwin and Chapple, 1968; Price and Cosgrove, 1990).

### ***Rheological ‘Thought Experiments’***

Layering of materials can affect strain accumulation and the distribution and orientation of structures observed at the surface. Two simple rheological layer models are deformed here in ‘thought experiments’ in order to explore possible differences in resulting surface morphologies.

In the first model (model A) a thin layer of relatively strong material sits above relatively weak material (Figure 16 A). The boundary between the two layers is defined

by a décollement. The decrease in relative strength between the two layers could be due to a change in composition or by an elevated geothermal gradient (implications for both discussed below). Both layers behave as ductile solids. With model bulk contraction the thin surface layer might accommodate strain by forming short-wavelength buckle folds whereas the subsurface accommodates strain by homogeneous thickening (Figure 16 C). Alternatively the thin surface layer might accommodate strain by homogeneously thickening which would leave no record. With model bulk extension the surface layer might form ductile pinch and swell structures or brittle boudins, whereas the subsurface accommodates strain by homogeneous thinning (Figure 16 D). Alternatively the thin layer might accommodate strain by homogeneously thinning, which would leave no record. If the surface behaves brittlely during bulk extension then fractures or boudins might form while the subsurface homogeneously thins (Figure 16 E). The resulting cross-sectional surface morphologies of both ductile cases, whether bulk contraction or bulk extension, are indistinguishable from one another, however the end-member brittle response is clearly different.

In the second model (model B) a thin relatively strong layer sits above a thicker and somewhat stronger layer, which is in turn underlain by a thick relatively weak layer (Figure 17 A). Décollements mark the boundaries between layers. All layers behave as ductile solids. With model bulk contraction the relatively strong subsurface layer buckles into long-wavelength folds whereas the weak layer below thickens homogeneously (Figure 17 C). The surface layer might deform differently along its length, depending on its location relative to the long-wavelength folds and the amount of accumulated strain

(Figure 17 B). The surface layer might locally extend at the crests and locally shorten in the troughs of the long-wavelength folds, and show no strain along the fold limbs. Surface layer local extension could be accommodated by homogeneous thinning or by the formation of pinch and swell structures. Local contraction could be accommodated by formation of folds, or homogeneous thickening, which would leave no record of strain.

With model bulk extension the relatively strong subsurface layer forms pinch and swell structures whereas the underlying weak layer thins homogeneously (Figure 17 D). Depending on total strain accumulation, the surface layer might locally extend where the underlying layer pinches, whereas little strain would accumulate above the swells. The resulting cross-sectional topographic morphologies of the two cases both display long-wavelength undulations. However, depending on the amount of total strain, we might expect to see a difference in short-wavelength lineaments. With bulk contraction short-wavelength lineaments would develop on the crests and troughs of long-wavelength folds and not along fold limbs whereas short-wavelength lineaments would only develop in the troughs of pinch and swell structures with bulk extension (Figure 17).

Comparing the two models allows us to determine if significant differences exist. The first-order difference between the results of the two thought experiment results is the development of long-wavelength topography. Long-wavelength topography forms with both bulk contraction and extension in model B. However long-wavelength structures are not predicted with either bulk contraction or extension in model A.

The second-order difference between the experiments is the distribution of short-wavelength structures. With bulk contraction in model B, short-wavelength structures can

form at the crests and troughs but are absent in the limbs of long-wavelength folds. Short-wavelength structures only form in the troughs of long-wavelength topography with extension. However, short-wavelength structures are expected to form across the entire surface with bulk contraction in model A. Therefore the presence of gaps or punctuated spacing of short-wavelength structures, especially if associated with long-wavelength topography, favors model B conditions.

A note of caution: these models are simple thought experiments and carry with them a number of caveats. The models are not a quantitative assessment nor are they derived from rigorous numerical modeling. The flow laws for the hypothetical materials are not considered except to assume that pressure/temperature conditions and strain rate are within the realm where the materials will behave as described in each model (i.e. brittle vs. ductile). The thought experiments do not consider progressive development of folds which might serve to increase the effective mechanical thickness of a layer and thus increase fold wavelength. The models also assume plane strain with no change in volume.

### ***From Thought Experiments to Reality***

Recall that the penetrative fabric morphology as observed in *Magellan* SAR imagery consists of symmetric rounded ridges (Figure 15). The penetrative fabric displays consistent wavelengths across the entire interior and is not associated with parallel long-wavelength topography. The penetrative fabric is consistent in character across strike and does not display periodically spaced gaps. Therefore the penetrative fabric is most consistent with deformation of a laterally extensive, thin and relatively



strong layer above a thick relatively weak layer that accommodated strain homogeneously as described above. Furthermore, the penetrative fabric is arguably inconsistent with deformation of a thick strong layer because of the lack of associated long-wavelength topography.

However, constraining the bulk strain of the penetrative fabric proves difficult. Model A produced rounded ridges through ductile processes in both bulk contraction and extension. A range of layer thickness can be estimated without direct constraint of the strain regime. Typical wavelength to thickness ratios ( $\lambda/H$ ) range from 1-6 for extensional and contractional deformation as stated above. The penetrative fabric wavelengths range from 300-952 m yielding layer thickness estimates of 50-1000 m.

The physical nature of a laterally extensive, thin, relatively strong layer is difficult to address. A compositional difference between layers provides one explanation. A compositional difference would require a mechanism to emplace a relatively uniform and thin layer of material across a very large area. Widespread sedimentation analogous to terrestrial ocean basin accumulation is one candidate. This requires liquid water to enhance erosion rates to create and transport sediment. Venus' surface presently lacks liquid water and significant erosion rates (Kaula, 1990), however conditions on Venus could have been very different in the past. The high deuterium/hydrogen ratio of Venus' atmosphere is consistent with past wet conditions (Donahue et al., 1982), which may have supported widespread erosion and deposition.

Flood-lava flows could also create a thin layer with a different composition. This would require widespread volcanism across the entire interior of Artemis, low-viscosity

lava, and presumably magma storage across a large area. The presence of a large subsurface magma chamber might be expressed by variation in the local strain regime, however the penetrative fabric is consistent in character and orientation across the entire interior. Numerous small magma chambers or point sources of magma distributed across Artemis could provide source material with less influence on the local accumulation of strain. It is possible and even likely that the development of penetrative fabric and later tectonic deformation overprinted the surface expression of the magma chambers.

Alternatively, a rheologically-defined thin layer might result from locally elevated geothermal gradients which raise the regional brittle-ductile transition to shallow levels. Heating the shallow crust to high temperatures without melting could anneal the surface layer with time, thereby strengthening the layer. Elevated geothermal gradients might not result in a sharp décollement between the thin surface layer and the subsurface, however the importance of the width of this mechanical transition zone is unknown and a wider zone might be acceptable at the first order. Recent finite-element modeling of short-wavelength folding by contracting and cooling of ultra-dry diabase at surface temperatures temporarily elevated to 1000 K indicate that the high temperatures might threaten the competence of the thin layer, making formation and preservation of short-wavelength structures difficult (Ghent et al., 2005). However, the composition of Venusian crust is not well understood and could be much stronger, or weaker, than currently believed.

None of these scenarios can be robustly eliminated with currently available data and other explanations might exist. Future missions with higher resolution imagery and

topography data will help refine constraints on the penetrative fabric. Lander missions that provide robust geochemical data could also be helpful if the geologic context of their sampling is well constrained and understood.

## **Geologic history**

Artemis as a whole formed tectonically coherently with interior, chasma, and exterior regions evolving broadly contemporaneously. Across Artemis tectonic structures at all scales display a remarkable consistency in style and trend. Suites of chasma-parallel structures, radial fractures and wrinkle ridges each define circles with centers near the center of Artemis, strongly suggestive of a genetic relationship (Hansen, 2002). Here I consider the geologic evolution of the interior region and attempt to relate it to the formation of Artemis Chasma.

Artemis' interior units roughly divide into two groups: 1) high-backscatter, highly tectonized terrains (units btaA and btbA) and 2) low-backscatter, relatively smooth volcanic flow materials (units fcaA, fcbA, sfaA, sfbA, sfcA, fu, and lfu). The penetrative tectonic fabric found in units btaA and btbA displays a consistent northeast trend throughout the interior. Radial and concentric structural suites and associated lava flows define four centers of tectonic and magmatic activity.

The penetrative fabric represents the locally oldest observable signature of tectonic deformation (Figure 18). Although the onset of penetrative fabric formation is unconstrained, the main phase of penetrative fabric formation appears to have broadly ended relatively early in Artemis' interior history. Penetrative fabric formation requires the creation and subsequent deformation of a thin mechanically-defined layer across the interior of Artemis. Penetrative fabric formation overlapped in time and space with tectonism of units btaA and btbA related to the four tectonomagmatic centers. As I will

show below, cross-cutting relationships indicate that the development of penetrative fabric broadly ended earlier than the development of the tectonomagmatic centers.

The four tectonomagmatic centers preserve a complex history of locally centralized deformation and volcanism that temporally and spatially overlap one another. Volcanic flows emanating from TMa cover flows emanating from TMb, and vice versa, indicating broadly contemporaneous emplacement of these two centers. The flows also locally bury preexisting structures related to the tectonomagmatic centers. Lineaments in the volcanic flows show similar trends as the penetrative fabric; thus these lineaments likely represent reactivation of penetrative fabric structures. Volcanic flows in unit fcbA, located between TMc and TMd, are difficult to individually delineate and thus to attribute to one tectonomagmatic center over the other. Likewise, volcanic flows in unit fcbA appear to emanate from TMb and flow towards TMc, and vice-versa; however, no discrete boundary exists between opposing flows which appear to laterally grade into each other. These relationships indicate broadly synchronous or time-transgressive emplacement of these units at the scale of the map. It seems clear however, that the bulk of the tectonomagmatic center deformation predated the bulk of composite flow formation.

The shield fields at the centers of TMa, TMb, and TMc (units sfaA, sfbA, and sfcA respectively) locally bury preexisting structures related to their respective tectonomagmatic center and are in turn deformed by them (Figure 19). These relationships indicate that the bulk of the individual shield fields' formation occurred as tectonomagmatic center deformation waned. No robust temporal relations exist between

the evolution of the shield fields and the composite flows because these map units are not in contact with one another.

The pervasive development of Artemis Chasma topography and chasma structures prohibits robust correlations of interior units to exterior units. The discrete chasma boundary locally truncates unit btaA in the southwest and northeast. Structures associated with the tectonomagmatic centers do not appear to cut chasma structures, indicating either: 1) chasma deformation is broadly younger than, and overprinted, the basal terrain deformation; or 2) the local strain regime near the chasma did not favor development of broadly contemporaneous basal terrain structures. Unit fcbA appears to embay the chasma along parts of the contact (Figure 20). However some chasma-parallel structures near impact crater Behn cut fcbA, whereas other chasma-parallel structures in the area appear flooded by unit fcbA (Figure 20 B). These relationships are consistent with broadly contemporaneous formation of the chasma and unit fcbA. Unit fcaA locally covers part of the chasma. Shallow troughs related to TMa cut, and are cut by, chasma-parallel structures, indicating a broadly contemporaneous and time-transgressive relationship (Figure 21).

Figure 22 summarizes the development of Artemis' interior described above with a cartoon block diagram. The interior region is the focus of this research and, as such, deformation in the exterior is not addressed in the block diagram. Artemis' interior history is anything but linear, yet shows a general progression from relatively early widespread tectonism associated with penetrative fabric formation to locally focused tectonism and volcanism associated with tectonomagmatic center evolution. Artemis'

interior and Artemis Chasma evolved broadly contemporaneously, although the onset and duration of chasma formation relative to the interior deformation is not constrained.

## **Evaluation of hypotheses**

Four published hypotheses have been proposed for Artemis formation: subduction, metamorphic core complex, bolide impact, and deep mantle plume. Figure 23 summarizes some of the testable predictions of each hypothesis as discussed below.

### ***Subduction hypothesis***

The subduction hypothesis was proposed by various authors who noted the topographic similarity of Artemis Chasma to terrestrial subduction trenches (McKenzie et al., 1992; Brown and Grimm, 1995; Schubert and Sandwell, 1995; Brown and Grimm, 1996). This hypothesis suggests northwest-southeast directed convergence and underthrusting of ~250 km of exterior plains under the interior region of Artemis. The postulated subducted slab would likely lack water for magmatic fluxing (Kaula, 1990), and locally depress the geothermal gradient. Therefore, upper-plate volcanic activity would not be expected, in contrast to terrestrial subduction zones. According to the subduction hypothesis the topographic expression of Artemis Chasma results from flexure of the down-going slab. However, flexure does not appear to be an adequate explanation for the topographic expression of the entire chasma. Plates should slip past each other rather than over/under ride one another where their common boundary is subparallel to the direction of convergence. Therefore flexure should not occur where the chasma axis trends northwest or southeast.

The subduction hypothesis makes a number of testable predictions, each of which are briefly stated and then evaluated or tested in light of the geologic mapping and history presented above.



*Prediction:* Chasma-parallel normal faults might be expected to form in an outer rise.

*Test:* Chasma-parallel normal faults are not observed in the outer rise (Brown and Grimm, 1995; Hansen, 2002). Flexural modeling obtained reasonable fits for the southeastern portion of Artemis Chasma though it required a high in-plane force to prevent brittle failure in the outer rise (Brown and Grimm, 1996).

*Prediction:* Artemis Chasma should record left-lateral strike-slip displacement along its northeast portion and right-lateral strike-slip displacement along its southwest portion.

*Test:* Hansen (2002) found that geologic evidence in the northeast part of the chasma is inconsistent with left-lateral strike-slip motion and the reader is referred to that work for a detailed discussion. Brown and Grimm (1995) interpreted right-lateral shear in a north-northwest-trending deformation belt at the southwest margin of TMa. This interpretation is based, in part, on the observation of a change in trend of lineaments as they cross a ridge with significant relief (Figure 24). However, the apparent change in trend coincides with a relatively sharp topographic rise and likely results from radar foreshortening, rather than true displacement. Radar foreshortening would displace areas of high topography (in this case the north side of the slope break) towards the radar illumination source resulting in an apparent change in trend (Figure 24). Thus the apparent bend in lineaments might be best interpreted as a radar imaging artifact. Even if one accepts the apparent lineament trend as real, the resulting geometry is inconsistent with a right-lateral shear interpretation. Figure 24 illustrates predicted lineament

geometries for: a) shear of preexisting lineaments, b) extensional fractures, and c) contractional structures that form progressively during both left- and right-lateral simple-shear deformation. The only scenarios that produce the observed lineament geometries are left-lateral simple shear of preexisting lineaments and extensional structures formed during progressive left-lateral simple-shear deformation. Left-lateral simple shear is the opposite displacement predicted by the subduction hypothesis. Therefore the lineaments across the ridge are difficult to reconcile with the subduction hypothesis.

Further evidence against a right-lateral displacement interpretation exists to the west along the chasma. Here a suite of roughly east-trending lineaments that represent shallow troughs interact with chasma structures. In some cases the shallow troughs cut the chasma lineaments; in other cases the chasma lineaments cut the shallow troughs. Yet nowhere do the shallow troughs appear horizontally displaced across the chasma. These relations indicate broadly contemporaneous formation of shallow troughs and chasma lineaments (Figure 21).

*Prediction:* Interior volcanic deposits and associated deformation features should predate the initiation of convergence and subduction.

*Test:* Composite flow unit fcaA, probably genetically related to TMa, extends across the western margin of the chasma. Cross-cutting relationships are consistent with broadly contemporaneous formation of TMa and at least a portion of Artemis Chasma as stated above. In addition, unit fcbA, probably related to TMb and TMc, appears to embay the chasma along much of the southeastern margin. Chasma-parallel lineaments, near impact crater Behn, deform unit fcbA and yet also variably display evidence of burial by

unit fcbA. Small chasma-parallel ridges in unit fcbA near the southeast margin may represent inversion structures or reactivation of buried fractures. These relationships indicate that the interior volcanic activity temporally overlapped to some extent with formation of the chasma, at least at two locations. Therefore interior volcanic activity does not completely predate subduction, as predicted.

*Prediction:* The postulated subducted slab should contribute to a gravity anomaly on the concave side of the subduction zone resulting in a shallow apparent depth of compensation.

*Test:* A semi-circular positive gravity anomaly exists in the concave side of the hypothesized subduction zone (Figure 5). A best fit apparent depth of compensation of  $200 \pm 12.5$  km for the large gravity anomaly and about  $50 \pm 12.5$  km for the Artemis region in general is consistent with thickened crust, partial dynamic support, or a combination thereof (Schubert et al., 1994; Simons et al., 1997). The solutions are non-unique, therefore the data allow, but do not require, the prediction (Schubert et al., 1994; Simons et al., 1997).

*Verdict:* The predictions of the subduction hypothesis addressed here are generally inconsistent with geological observations. Moreover, the subduction hypothesis does not address the formation of the pervasive penetrative fabric. The subduction hypothesis does not provide a robust explanation for the formation of Artemis.

### ***Metamorphic core complex hypothesis***

The metamorphic core complex hypothesis suggests Artemis records a composite structure. In this hypothesis the interior represents a metamorphic core complex, marking

exposure of a ductily-deformed crust (Spencer, 2001). The hypothesis is based on an analysis of deformation in a limited portion of the interior of Artemis. According to the hypothesis the interior of Artemis exposes deep crustal rocks due to 170 km of northwest-southeast directed extension. The hypothesis does not place this 170 km of crustal extension into a regional context and, as such, specific predictions are difficult to delineate. However, the lack of significant erosion on the surface of Venus (Arvidson et al., 1992) makes exhumation of deep crustal rocks unlikely and proves challenging for the metamorphic core complex hypothesis. In addition, the metamorphic core complex hypothesis does not address the formation of the pervasive penetrative fabric. The metamorphic core complex hypothesis limits deep-crustal extension to a small part of Artemis, however the penetrative fabric is preserved across this relatively small region of postulated exposure of deep crustal material and beyond with no apparent change in character.

### ***Bolide impact hypothesis***

The bolide impact hypothesis suggests that Artemis marks the surface expression of a huge bolide impact that formed no later than 3.9 Ga (Hamilton, 2005). As published, this hypothesis makes few specific predictions about Artemis, leaving the reader to speculate on important details. Typical predictions that might be inferred for such a large bolide impact follow.

*Prediction:* Artemis should display rimmed basin topography and a multi-ring structure typical of large impact craters on rocky targets (e.g. Wilhelms, 1973).

*Test:* Artemis' topography is an interior high surrounded by a trough and does not display multiple ring structures (Figure 25). In fact Artemis shows an inverse of the predicted topography, as illustrated by comparison of Artemis topography with the well accepted impact basin Hellas Planitia on Mars (Figure 26). Hellas Planitia forms an ~2000 km diameter basin with ~10 km relief. Although Venus and Mars are very different geologically, huge impact basins on both planets, as well as the Earth, should be negative topographic features unless a strong geophysical reason exists to believe otherwise (e.g. Jones et al., 2005).

*Prediction:* Preexisting structures in the interior of Artemis would have been obliterated by the bolide impact; therefore, interior deposits and structures should strictly post-date the formation of the crater rim.

*Test:* Geological observations discussed above indicate deformation in the interior of Artemis was, at least in part, broadly contemporaneous with formation of Artemis Chasma. These observations are inconsistent with this prediction.

*Prediction:* The crater 'rim' (Artemis Chasma) should form a complete circle. However no topographic expression exists along the northwest margin of Artemis. Hamilton (2005) suggested that the northwest 'rim' of the postulated impact crater was subsequently buried by thick sediment.

*Test:* Artemis chasma narrows and shallows tracing clockwise from the southeast. Chasma-related structures fade along with the diminishing topographic expression. There is no evidence of embayment, which would be expected in the case of burial. The interaction of shallow troughs and chasma lineaments in this area as noted above do not

display any obvious strain partitioning or deflection that might be expected if a significant crustal anisotropy such as a buried chasma were present. There is no evidence that the chasma formed a complete circle, which experienced later burial along its northwest trace.

*Verdict:* The bolide impact hypothesis is poorly developed and lacks such salient predictions as the size of bolide, the thickness and rheology of the lithosphere at time of impact, or the possible role of impact-induced melting. This hypothesis does not address the formation of the pervasive penetrative fabric, nor does it address the formation of the tectonomagmatic centers. If significant impact melt were generated, a thin layer may result in which penetrative fabric could develop, yet the consistent northeast trend would not be predicted. Ultimately the bolide impact hypothesis, as published, is not a viable explanation for the formation of Artemis and would require further development in light of the geologic constraints presented herein.

### ***Plume hypothesis***

The plume hypothesis suggests that Artemis represents the surface expression of a deep mantle plume (Griffiths and Campbell, 1991; Smrekar and Stofan, 1997; Hansen, 2002). This hypothesis initially arose from lab experiments aimed at modeling the interaction of a thermally-driven plume with the lithosphere (Griffiths and Campbell, 1991), and from later numerical modeling aimed at modeling corona formation (Smrekar and Stofan, 1997). Both physical and numerical models resulted in the formation of circular troughs similar to Artemis Chasma. Griffiths and Campbell (1991) also noticed that their physical plume models developed small-scale convection cells, which

compartmentalized the interior of a flattening plume. This is analogous to the segmentation of Artemis' interior region into localized tectonomagmatic centers. As an alternative to small-scale convection cells Hansen (2002) proposed the formation of smaller compositionally or thermally driven diapirs above a flattening plume head to accommodate internal localized tectonomagmatic centers. Numerical modeling of diapirs also resulted in raised interior topography and subsequent collapse of topography (Koch and Manga, 1996; Smrekar and Stofan, 1997). The plume hypothesis also accommodates crustal heterogeneity which may partition strain and prevent idealized map patterns from developing. The plume hypothesis makes the following predictions.

*Prediction:* Artemis Chasma formed as a coherent entity broadly synchronous with interior volcanic deposits and deformation, and deformation in the exterior.

*Test:* The continuity of chasma structures, radial fractures and concentric wrinkle ridges in the exterior strongly suggest a genetic relationship and broadly contemporaneous formation. As noted above, interior deformation and volcanic deposits formed broadly synchronously with the chasma. These observations are consistent with this prediction.

*Prediction:* Artemis' topography should reflect a raised interior region.

*Test:* The topography of Artemis, a raised interior region surrounded by a 1-2 km deep chasma, is consistent with this prediction.

*Prediction:* The postulated mantle plume would contribute to a gravity anomaly at Artemis resulting in a deep apparent depth of compensation.

*Test:* As discussed above, a semi-circular positive gravity anomaly exists at Artemis (Figure 5). The best fit apparent depth of compensation for the anomaly and the Artemis region in general are consistent with thickened crust, partial dynamic support, or a combination thereof (Schubert et al., 1994; Simons et al., 1997). These solutions are non-unique, however the gravity data are consistent with the prediction.

*Verdict:* While the plume hypothesis predictions are generally consistent with geologic and geophysical observations, this hypothesis does not address the pervasive penetrative fabric. A plume might transport enough heat to the surface to raise the brittle-ductile transition to shallow depths to create a thin layer for the penetrative fabric to form, yet it is not intuitively obvious why a strong preferred northeast fabric orientation would form. The plume hypothesis is the most promising hypothesis currently entertained, however it requires modification to explain the penetrative fabric.



## **Conclusions**

The interior region of Artemis records a rich history of spatially and temporally evolving tectonism and volcanism. Artemis' interior region was deformed broadly synchronously with Artemis Chasma and Artemis' exterior region. The pervasive penetrative tectonic fabric in the interior region of Artemis imposes strong constraints on any hypothesis for Artemis' formation. The penetrative fabric requires the relatively early formation of a thin mechanically defined layer 10's to 100's of meters thick that was subsequently deformed. None of the hypotheses for Artemis formation presented here account for the formation of the penetrative fabric. The plume hypothesis is the most promising hypothesis currently entertained, as it can account for the formation of Artemis chasma and the tectonomagmatic centers in a coherent tectonic framework. However the plume hypothesis must be modified to address the formation of the penetrative fabric.

## References

- Arvidson, R. E., Greeley, R., Malin, M. C., Saunders, R. S., Izenberg, N., Plaut, J. J., Stofan, E. R., and Shepard, M. K., 1992, Surface modification of Venus as inferred from Magellan observations of plains: *Journal of Geophysical Research*, v. 97, no. E8, p. 13303-13317.
- Baker, V. R., Komatsu, G., Parker, T. J., Gulick, V. C., Kargel, J. S., and Lewis, J. S., 1992, Channels and valleys on Venus; preliminary analysis of Magellan data: *Journal of Geophysical Research*, v. 97, no. E8, p. 13,421-13,444.
- Barsukov, V. L., Volkov, V. P., and Khodakovsky, I. L., 1982, The crust of Venus; theoretical models of chemical and mineral composition: *Journal of Geophysical Research*, v. 87, Suppl., no. B1, p. A3-A9.
- Biot, M. A., 1961, Theory of folding of stratified viscoelastic media and its implications in tectonics and orogenesis: *Geological Society of America Bulletin*, v. 72, no. 11, p. 1595-1620.
- Brown, C. D., and Grimm, R. E., 1995, Tectonics of Artemis Chasma: a Venusian "plate" boundary: *Icarus*, v. 117, p. 219-249.
- , 1996, Lithospheric rheology and flexure at Artemis Chasma, Venus: *Journal of Geophysical Research*, v. 101, no. E5, p. 12697-12708.
- Donahue, T. M., Hoffman, J. H., Hodges, R. R., Jr., and Watson, A. J., 1982, Venus was wet; a measurement of the ratio of deuterium to hydrogen: *Science*, v. 216, no. 4546, p. 630-633.
- Ford, J. P., Plaut, J. J., Weitz, C. M., Farr, T. G., Senske, D. A., Stofan, E. R., Michaels, G., and Parker, T. J., 1993, Guide to Magellan image interpretation: Pasadena, California, National Aeronautics and Space Administration Jet Propulsion Laboratory, 148 p.
- Ghent, R. R., Phillips, R. J., Hansen, V. L., and Nunes, D. C., 2005, Finite element modeling of short-wavelength folding on Venus: Implications for the plume hypothesis for crustal plateau formation: *Journal of Geophysical Research*, v. 110, no. E11006, p. doi:10.1029/2005JE002522.
- Griffiths, R. W., and Campbell, I. H., 1991, Interaction of mantle plume heads with the Earth's surface and onset of small-scale convection: *Journal of Geophysical Research*, v. 96, no. B11, p. 18,295-18,310.
- Grimm, R. E., and Hess, P. C., 1997, The crust of Venus, *in* Bouger, S. W., Hunten, D. M., and Phillips, R. J., eds., *Venus II*: Tucson, University of Arizona Press, p. 1205-1244.

- Guest, J. E., Bulmer, M. H., Aubele, J. C., Beratan, K. K., Greeley, R., Head, J. W., Michaels, G., Weitz, C. M., and Wiles, C., 1992, Small volcanic edifices and volcanism in the plains of Venus: *Journal of Geophysical Research*, v. 97, no. E10, p. 15,949-15,966.
- Hamilton, V. E., and Stofan, E. R., 1996, The geomorphology and evolution of Hecate Chasma, Venus: *Icarus*, v. 121, p. 171-194.
- Hamilton, W. B., 2005, Plumeless Venus preserves an ancient impact-accretionary surface, *in* Foulger, G. R., Natland, J. H., Presnall, D. C., and Anderson, D. L., eds., *Plates, Plumes, and Paradigms: GSA Special Paper 388*, p. 781-814.
- Hansen, V. L., 2000, Geologic mapping of tectonic planets: *Earth and Planetary Science Letters*, v. 176, no. 3-4, p. 527-542.
- , 2002, Artemis; surface expression of a deep mantle plume on Venus: *Geological Society of America Bulletin*, v. 114, no. 7, p. 839-848.
- Ivanov, M. A., and Head, J. W., 2003, Evolution of three largest coronae on Venus, Heng-O, Quetzalpetlatl, and Artemis: Preliminary Results: XXXIV Lunar and Planetary Science Conference, no. 1188.pdf.
- Jones, A. P., Wuenemann, K., and Price, G. D., 2005, Modeling impact volcanism as a possible origin for the Ontong Java Plateau: *Special Paper - Geological Society of America*, v. 388, p. 711-720.
- Kaula, W. M., 1990, Venus; a contrast in evolution to Earth: *Science*, v. 247, no. 4947, p. 1191-1196.
- Kirk, R. L., 1993, Separation of topographic and intrinsic backscatter variations in bisopic radar images; a 'magic airbrush': *Proceedings of the Lunar and Planetary Science Conference*, v. 24, p. 803-804.
- Kirk, R. L., Soderblom, L. A., and Lee, E. M., 1992, Enhanced visualization for interpretation of Magellan radar data; supplement to the Magellan special issue: *Journal of Geophysical Research*, v. 97, no. E10, p. 16,371-16,380.
- Koch, D. M., and Manga, M., 1996, Neutrally buoyant diapirs; a model for Venus coronae: *Geophysical Research Letters*, v. 23, no. 3, p. 225-228.
- Komatsu, G., and Baker, V. R., 1994, Meander properties of Venusian channels: *Geology Boulder*, v. 22, no. 1, p. 67-70.
- Lang, N. P., and Hansen, V. L., 2006, Venusian channel formation as a subsurface process: *Journal of Geophysical Research*, v. in press.

- McDaniel, K., 2005, Circular lows, a genetically distinct subset of coronae? [masters thesis]: University of Minnesota Duluth, 79 p.
- McDaniel, K., and Hansen, V. L., 2005, Circular lows, a genetically distinct subset of coronae? [abs.]: XXXVI Lunar and Planetary Science Conference, no. 2367.pdf.
- McKenzie, D., Ford, P. G., Johnson, C. L., Parsons, B., Sandwell, D. T., Saunders, R. S., and Solomon, S. C., 1992, Features on Venus generated by plate boundary processes: *Journal of Geophysical Research*, v. 97, no. E8, p. 13533-13544.
- Okubo, C. H., and Martel, S. J., 1998, Pit crater formation on Kilauea Volcano, Hawaii: *Journal of Volcanology and Geothermal Research*, v. 86, no. 1-4, p. 1-18.
- Phillips, R. J., and Hansen, V. L., 1994, Tectonic and magmatic evolution of Venus: *Annual Review of Earth and Planetary Sciences*, v. 22, p. 597-654.
- Pollard, D. D., and Aydin, A., 1988, Progress in understanding jointing over the past century: *Geological Society of America Bulletin*, v. 100, no. 8, p. 1181-1204.
- Price, N. J., and Cosgrove, J. W., 1990, Analysis of geological structures.
- Ramberg, H., 1955, Natural and experimental boudinage and pinch-and-swell structures: *Journal of Geology*, v. 63, no. 6, p. 512-526.
- Rosenblatt, P., Pinet, P. C., and Thouvenot, E., 1994, Comparative hypsometric analysis of Earth and Venus: *Geophysical Research Letters*, v. 21, no. 6, p. 465-468.
- Sandwell, D. T., and Schubert, G., 1992, Flexural ridges, trenches, and outer rises around coronae on Venus: *Journal of Geophysical Research*, v. 97, no. E10, p. 16,069-16,083.
- Saunders, R. S., Spear, A. J., Allin, P. C., Austin, R. S., Berman, A. L., Chandler, R. C., Clark, J., deCharon, A. V., de Jong, E. M., Griffith, D. G., Gunn, J. M., Hensley, S., Johnson, W. T. K., Kirby, C. E., Leung, K. S., Lyons, D. T., Michaels, G. A., Miller, J., Morris, R. B., Morrison, A. D., Piereson, R. G., Scott, J. F., Shaffer, S. J., Slonski, J. P., Stofan, E. R., Thompson, T. W., and Wall, S. D., 1992, Magellan Mission summary: *Journal of Geophysical Research*, v. 97, no. E8, p. 13,067-13,090.
- Schubert, G., Moore, W. B., and Sandwell, D. T., 1994, Gravity over coronae and chasmata on Venus: *Icarus*, v. 112, no. 1, p. 130-146.
- Schubert, G., and Sandwell, D. T., 1995, A global survey of possible subduction sites on Venus: *Icarus*, v. 117, no. 1, p. 173-196.

- Sherwin, J.-A., and Chapple, W. M., 1968, Wavelengths of single-layer folds; a comparison between theory and observation: *American Journal of Science*, v. 266, no. 3, p. 167-179.
- Simons, M., Solomon, S. C., and Hager, B. H., 1997, Localization of gravity and topography; constraints on the tectonics and mantle dynamics of Venus: *Geophysical Journal International*, v. 131, no. 1, p. 24-44.
- Smrekar, S. E., and Stofan, E. R., 1997, Corona formation and heat loss on Venus by coupled upwelling and delamination: *Science*, v. 277, no. 5330, p. 1289-1294.
- Solomon, S. C., Head, J. W., Kaula, W. M., McKenzie, D. P., Parsons, B., Phillips, R. J., Schubert, G., and Talwani, M., 1991, Venus tectonics; initial analysis from Magellan: *Science*, v. 252, no. 5003, p. 297-312.
- Spencer, J. E., 2001, Possible giant metamorphic core complex at the center of Artemis Corona, Venus: *Geological Society of America Bulletin*, v. 113, no. 3, p. 333-345.
- Squyres, S. W., Janes, D. M., Baer, G., Bindschadler, D. L., Schubert, G., Sharpton, V. L., and Stofan, E. R., 1992, The morphology and evolution of coronae on Venus: *Journal of Geophysical Research*, v. 97, no. E8, p. 13,611-13,634.
- Stofan, E. R., Hamilton, V. E., Janes, D. M., and Smrekar, S. E., 1997, Coronae on Venus: morphology and origin, *in* Bouger, S. W., Hunten, D. M., and Phillips, R. J., eds., *Venus II*, University of Arizona Press, p. 931-968.
- Stofan, E. R., Sharpton, V. L., Schubert, G., Baer, G., Bindschadler, D. L., Janes, D. M., and Squyres, S. W., 1992, Global distribution and characteristics of coronae and related features on Venus; implications for origin and relation to mantle processes: *Journal of Geophysical Research*, v. 97, no. E8, p. 13,347-13,378.
- Surkov, Y. A., Kirnozov, F. F., Glazov, V. N., Dunchenko, A. G., Tatsy, L. P., and Sobornov, O. P., 1987, Uranium, thorium, and potassium in the Venusian rocks at the landing sites of Vega 1 and 2: *Journal of Geophysical Research*, v. 92, no. B4, p. E537-E540.
- Tanaka, K. L., Moore, H. J., Schaber, G. G., Chapman, M. G., Stofan, E. R., Campbell, D. B., Davis, P. A., Guest, J. E., McGill, G. E., Rogers, P. G., Saunders, R. S., and Zimbelman, J. R., 1994, *The Venus geologic mappers' handbook: Open-File Report - U. S. Geological Survey*.
- Vita-Finzi, C., Howarth, R. J., Tapper, S. W., and Robinson, C. A., 2005, Venusian craters, size distribution, and the origin of coronae, *in* Foulger, G. R., Natland, J. H., Presnall, D. C., and Anderson, D. L., eds., *Plates, Plumes, and Paradigms: GSA Special Paper 388*, p. 815-824.

Wilhelms, D. E., 1973, Comparison of Martian and Lunar Multiringed Circular basins: Journal of Geophysical Research, v. 78, no. 20, p. 4084-4095.

Zimelman, J. R., 2001, Image resolution and evaluation of genetic hypotheses for planetary landscapes: Geomorphology, v. 37, no. 3-4, p. 179-199.

	<b>Earth</b>	<b>Venus</b>
<b>Mass (kg)</b>	5.976 x 10 <sup>24</sup>	4.869 x 10 <sup>24</sup>
<b>Equatorial radius (km)</b>	6,378.14	6,051.8
<b>Mean density (gm/cm<sup>3</sup>)</b>	5.52	5.25
<b>Mean distance from the Sun (km)</b>	149,600,000	108,200,000
<b>Rotational period (days)</b>	0.99727	243.0187 (retrograde)
<b>Orbital period (days)</b>	365.256	224.701
<b>Equatorial surface gravity (m/sec<sup>2</sup>)</b>	9.78	8.87
<b>Satellites</b>	1	0
<b>Magnetic field</b>	Yes	No
<b>Mean surface temperature</b>	15° C	482° C
<b>Atmospheric pressure (bars)</b>	1.013	92
<b>Atmospheric composition</b>	N <sub>2</sub> - 77% O <sub>2</sub> - 21% Other - 2%	CO <sub>2</sub> - 96% N <sub>2</sub> - 3+% Trace amounts of: Sulfur dioxide, water vapor, carbon monoxide, argon, helium, neon, hydrogen chloride, and hydrogen fluoride

**Table 1. Summary of physical characteristics of the Earth and Venus.**

<b>Radar system characteristics</b>	
Wavelength	12.6 cm
Operating Frequency	2.385 GHz
Modulation Bandwidth	2.26 MHz
Transmitted pulse length	26.5 $\mu$ s
<i>SAR Antenna</i>	
Gain	36.0 dB
Angular beamwidth	2.1° x 2.5°
<i>Altimeter Antenna</i>	
Gain	19.0 dB
Angular beamwidth	10° x 30°
Polarization	HH
Effective slant-range resolution	88 m
Along-track resolution	120 m
<b>Orbit characteristics</b>	
Periapsis altitude	289 km
Periapsis latitude	9.5° N
Altitude at pole	2000 km
Inclination	85.5°
Period	3.259 hrs
Repeat cycle	243 days

**Table 2. Summary of Magellan radar and orbital characteristics.**



Latitude	Longitude	Transect (km)	Wavelength (m)	Orientation
-25.58	134.74	9.4	303	NE
-30.35	129.70	8.6	345	NE
-31.63	133.75	20.9	380	NE
-34.34	132.10	18.9	402	NE
-30.95	137.09	18.9	449	SE
-29.59	130.09	30.8	453	NE
-32.46	130.61	12.0	462	NE
-30.80	134.42	35.6	468	N
-27.57	136.65	21.7	494	NE
-32.15	130.93	27.2	495	NE
-35.38	133.62	32.1	526	NE
-30.71	130.64	45.8	572	NE
-30.78	129.99	58.2	588	NE
-36.21	132.48	44.3	607	NE
-28.12	136.09	85.9	641	NE
-35.83	132.13	48.0	657	NNE
-30.22	128.17	91.1	729	NE
-28.68	130.33	75.3	731	NE
-40.69	130.57	44.7	952	NE
Average			540 ± 157 (1σ)	
excluding outlier			517 ± 125 (1σ)	

**Table 3. Penetrative fabric wavelengths measured across Artemis.**

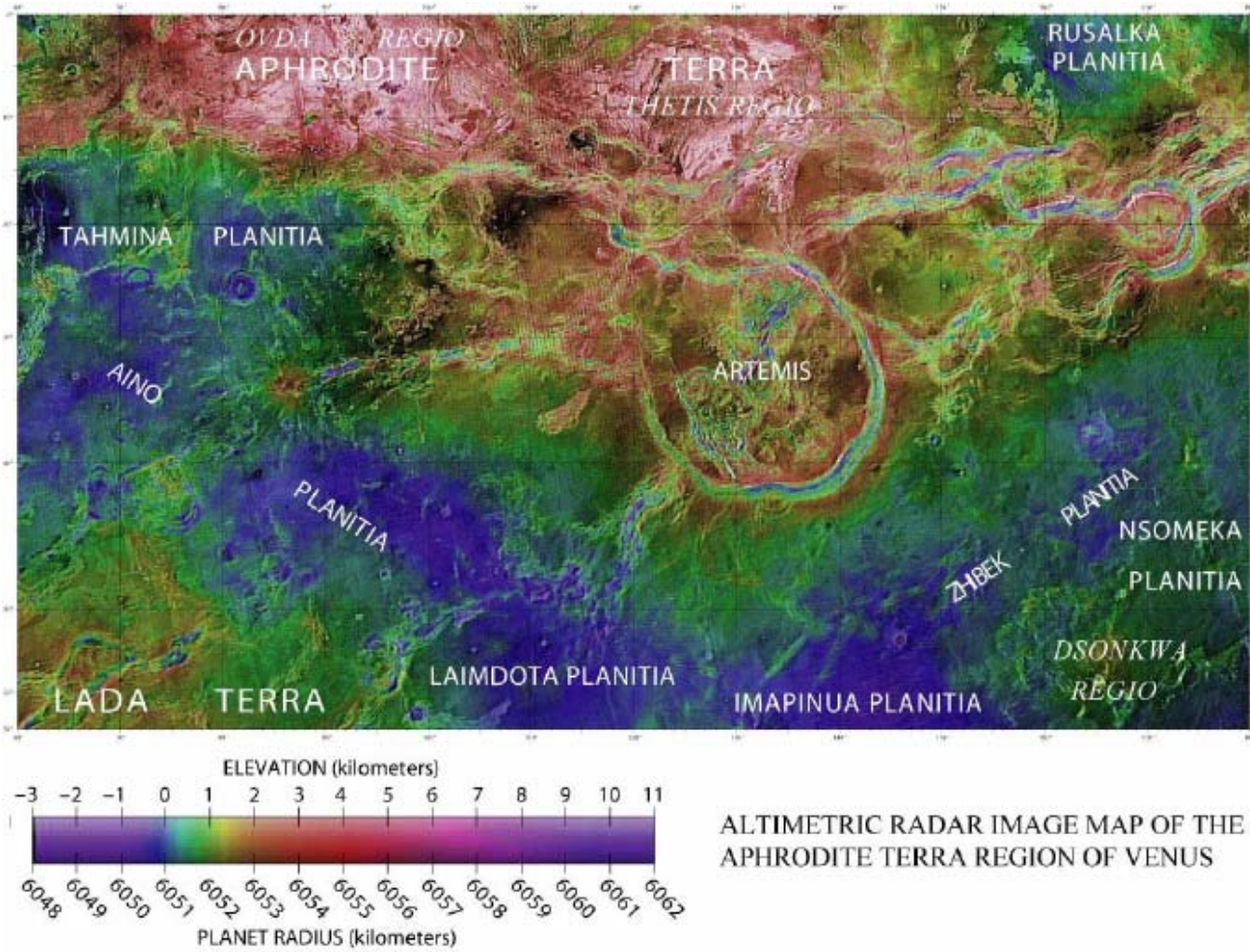


Figure 1. Regional altimetric radar map of Aphrodite Terra.

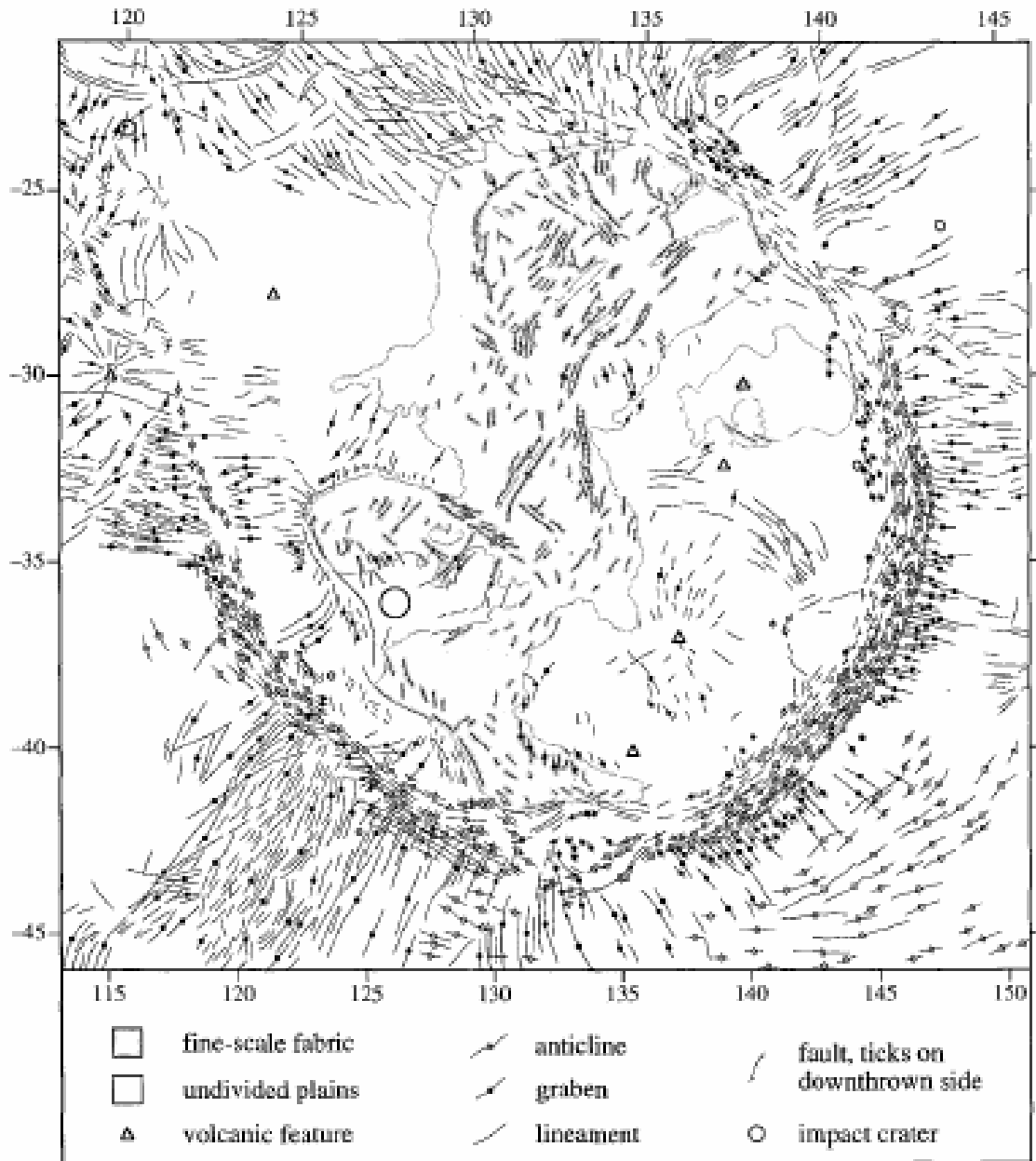


Figure 2. Tectonic sketch map of Artemis Chasma and vicinity (Brown and Grimm, 1995), condensed from mapping at 1:3,000,000 scale. Sinusoidal equal-area projection.

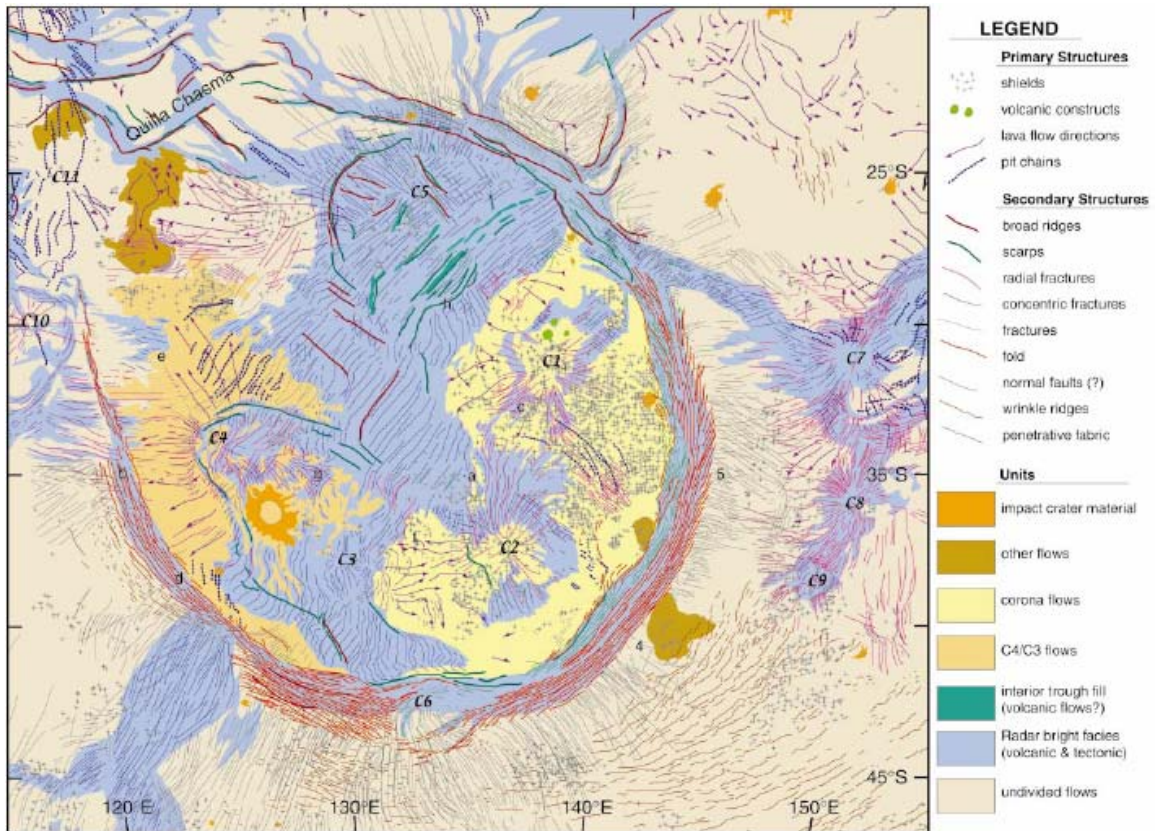


Figure 3. Geologic map of Artemis (Hansen, 2002; simplified from a compilation at 1:5,000,000 scale).

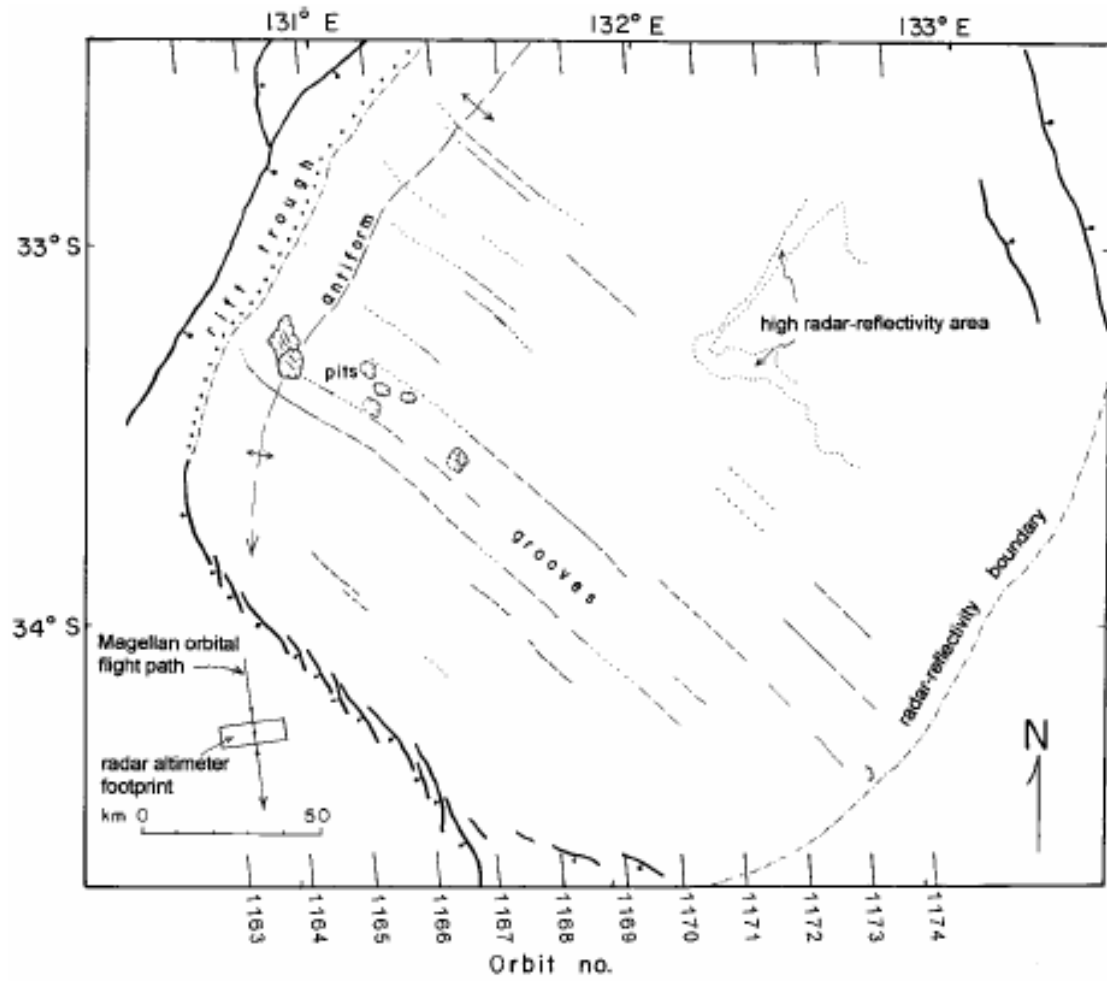


Figure 4. Interpretive map of major features associated with the grooved terrain at the center of Artemis (Spencer, 2001).



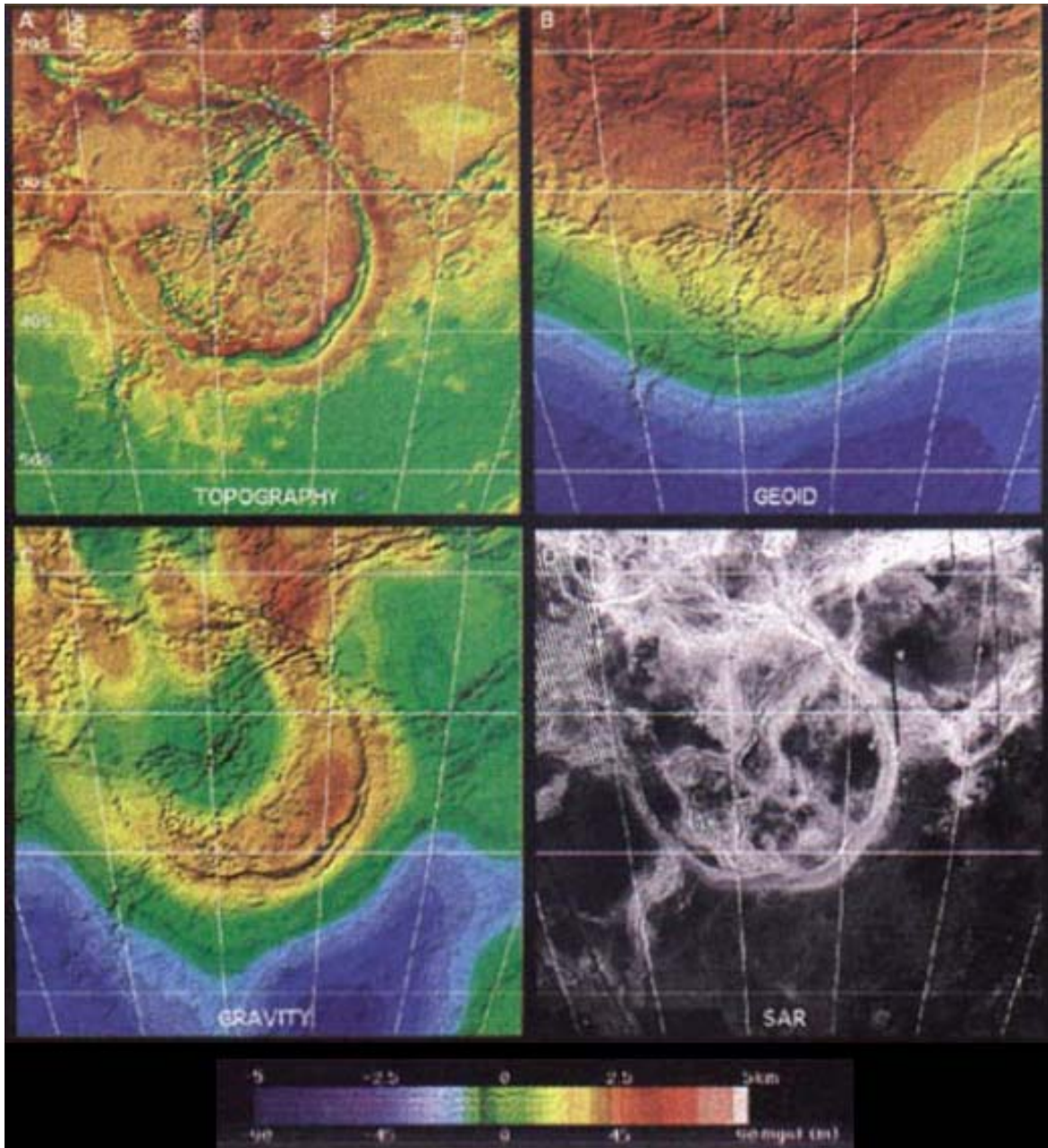


Figure 5. Gravity/topography data for Artemis (Schubert et al., 1994). A) Topography from gridded Magellan altimetry referenced to a mean planetary radius of 6051 km, B) geoid height from MGNP60FSAAP, 60th degree and order global spherical harmonic model, C) gravity anomaly from MGNP60FSAAP gravity model, D) Magellan SAR composite. The images are centered at 35°S, 135°E; latitude and longitude lines are plotted at 10° intervals.

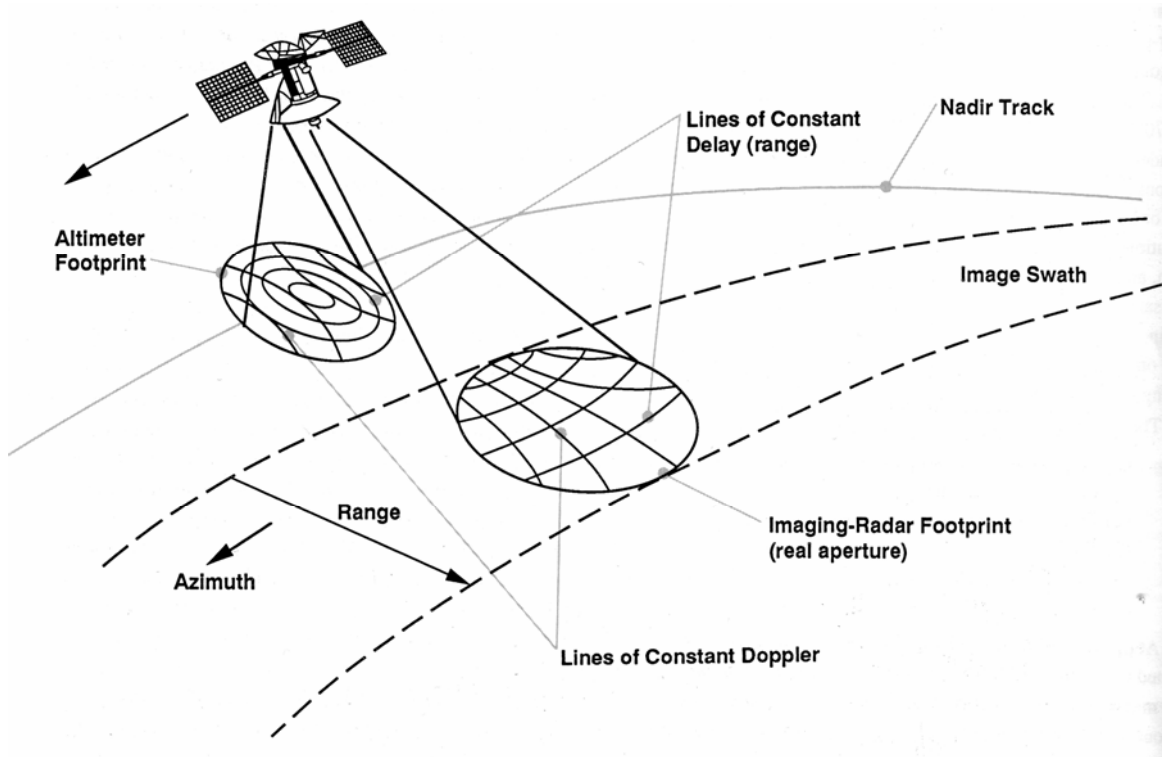
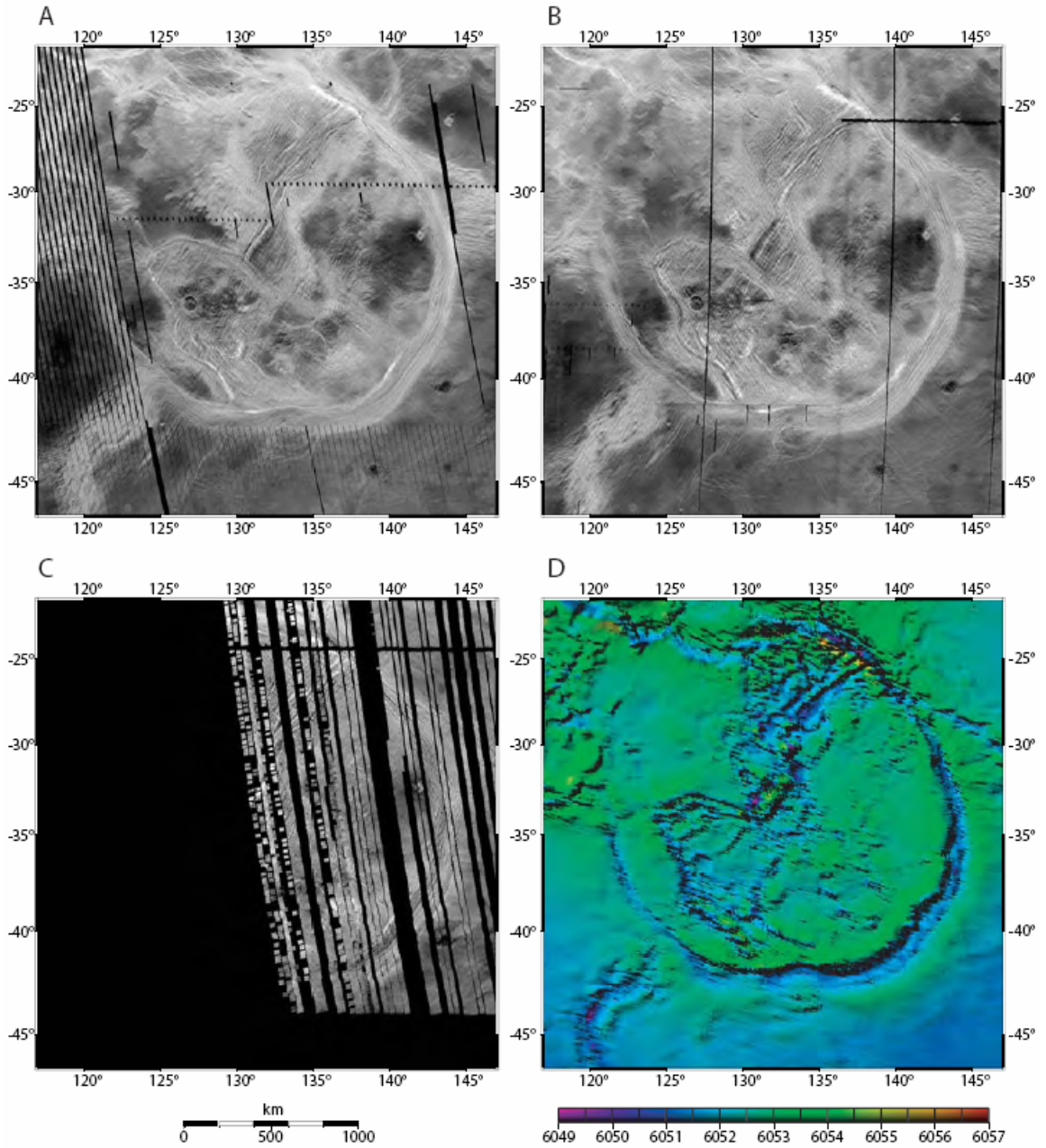


Figure 6. Magellan observing geometry. (Ford et al., 1993)



**Figure 7. Magellan data coverage for Artemis. A) Left-looking SAR, B) Right-looking SAR, C) Stereo left-looking SAR, D) Color-coded shaded relief derived from altimetry data. Black stripes indicate gaps in data coverage. SAR images have been stretched to enhance contrast.**



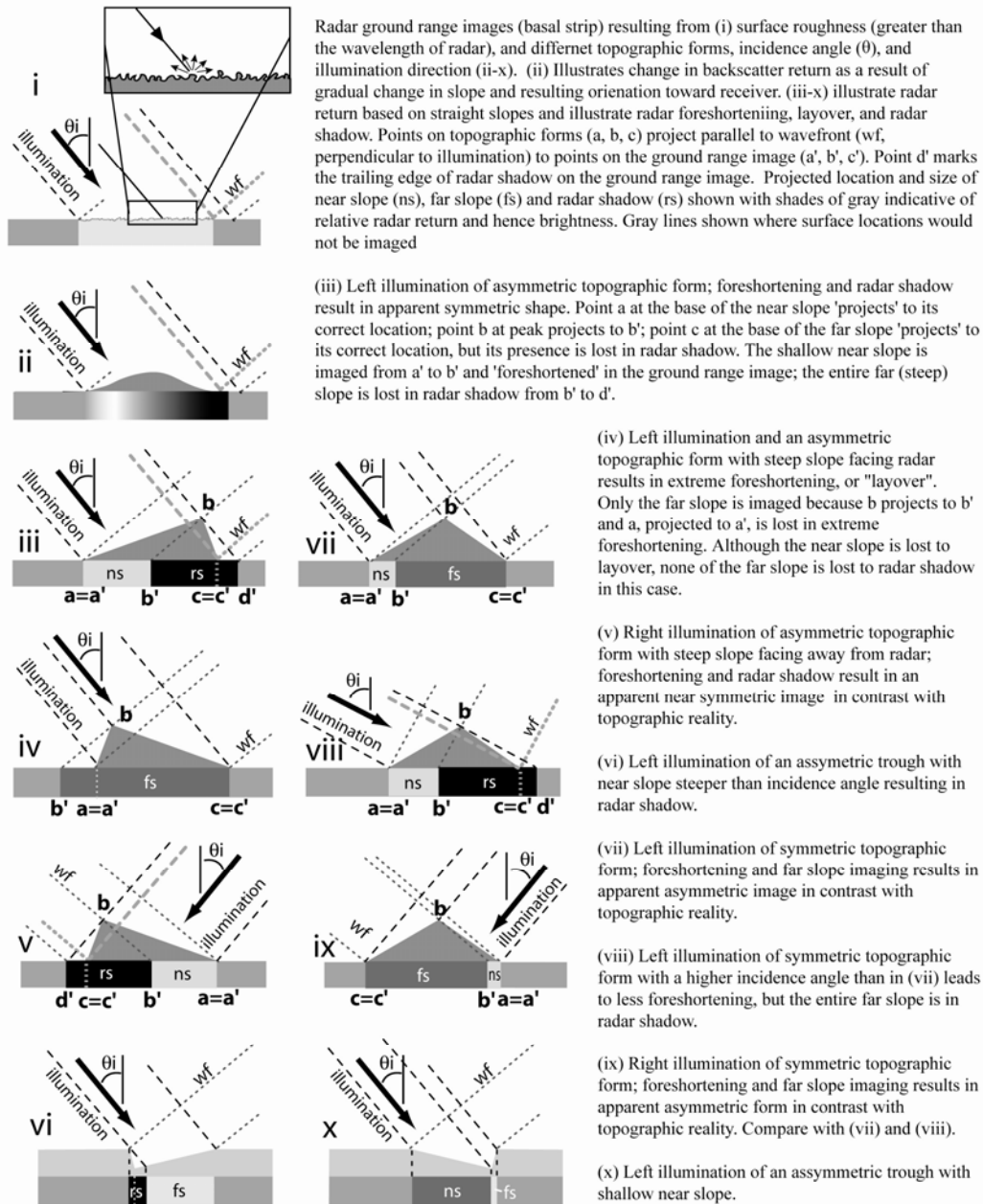
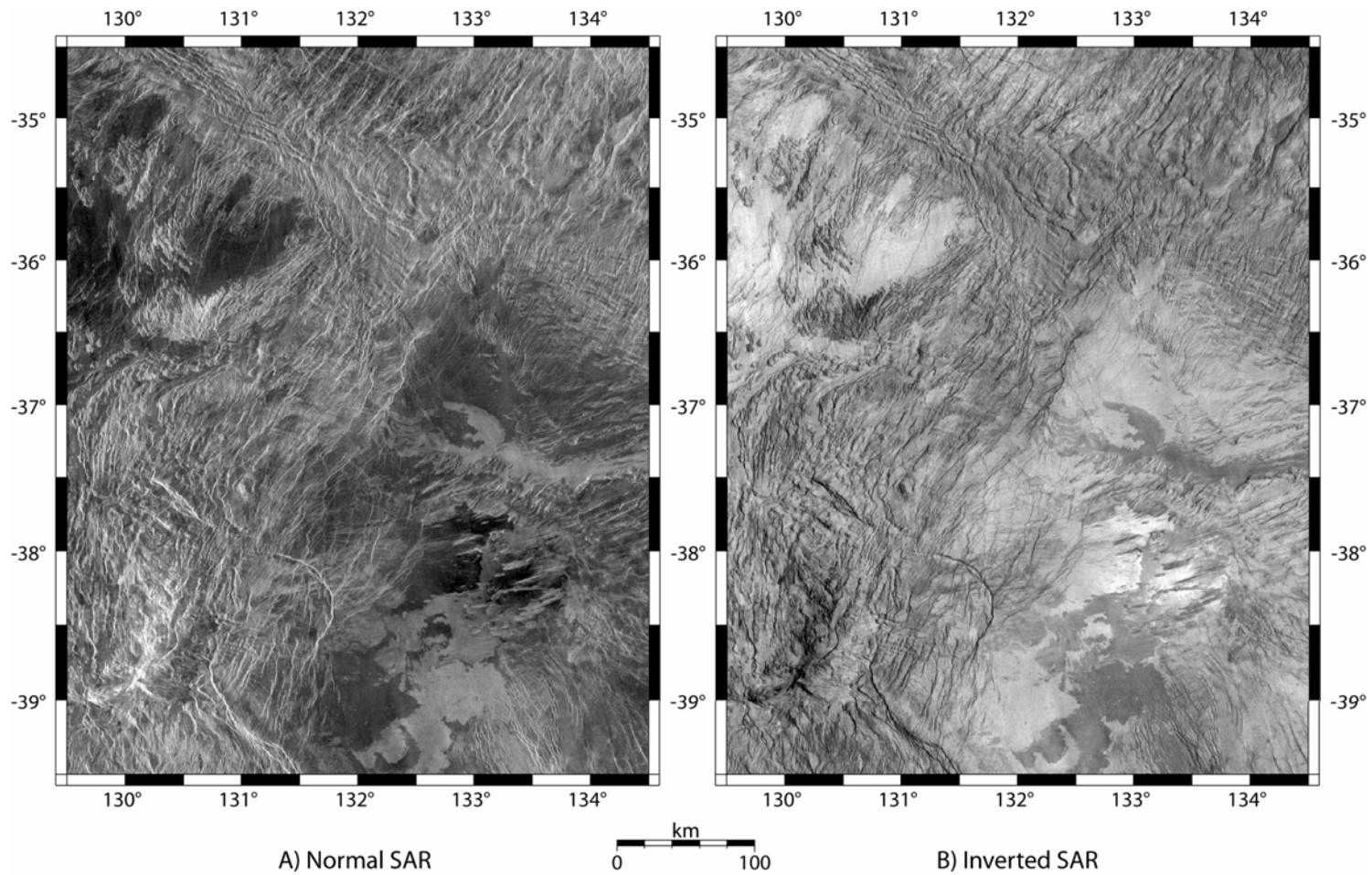
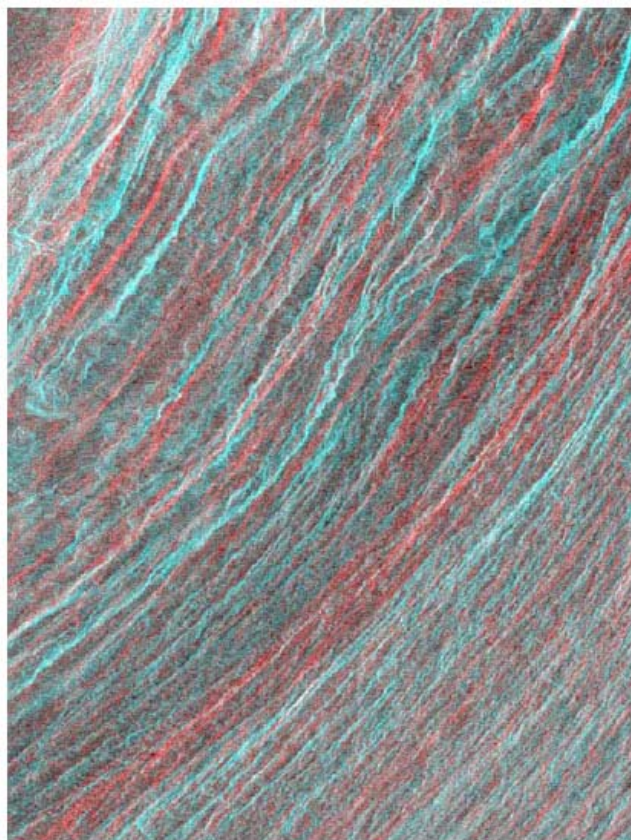


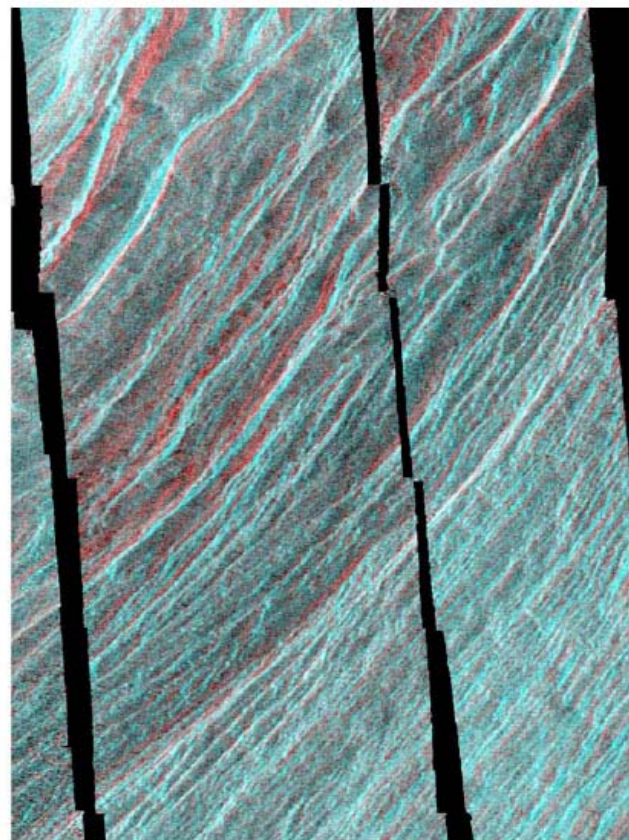
Figure 8. Various radar geometries. (Hansen, unpublished teaching materials).



**Figure 9. Comparison of normal and inverted SAR images. Structural lineaments such as fractures, folds, and faults are much easier to see in inverted images.**



A) Synthetic Stereo



B) True Stereo

Figure 10. Comparison of synthetic stereo images and true stereo images for the same area of Artemis Chasma. Long-wavelength topography is visible in synthetic stereo (A), whereas subtle short-wavelength topography along the trench wall is more apparent in true stereo (B). Black areas represent data gaps. Images are approximately 100 km across.

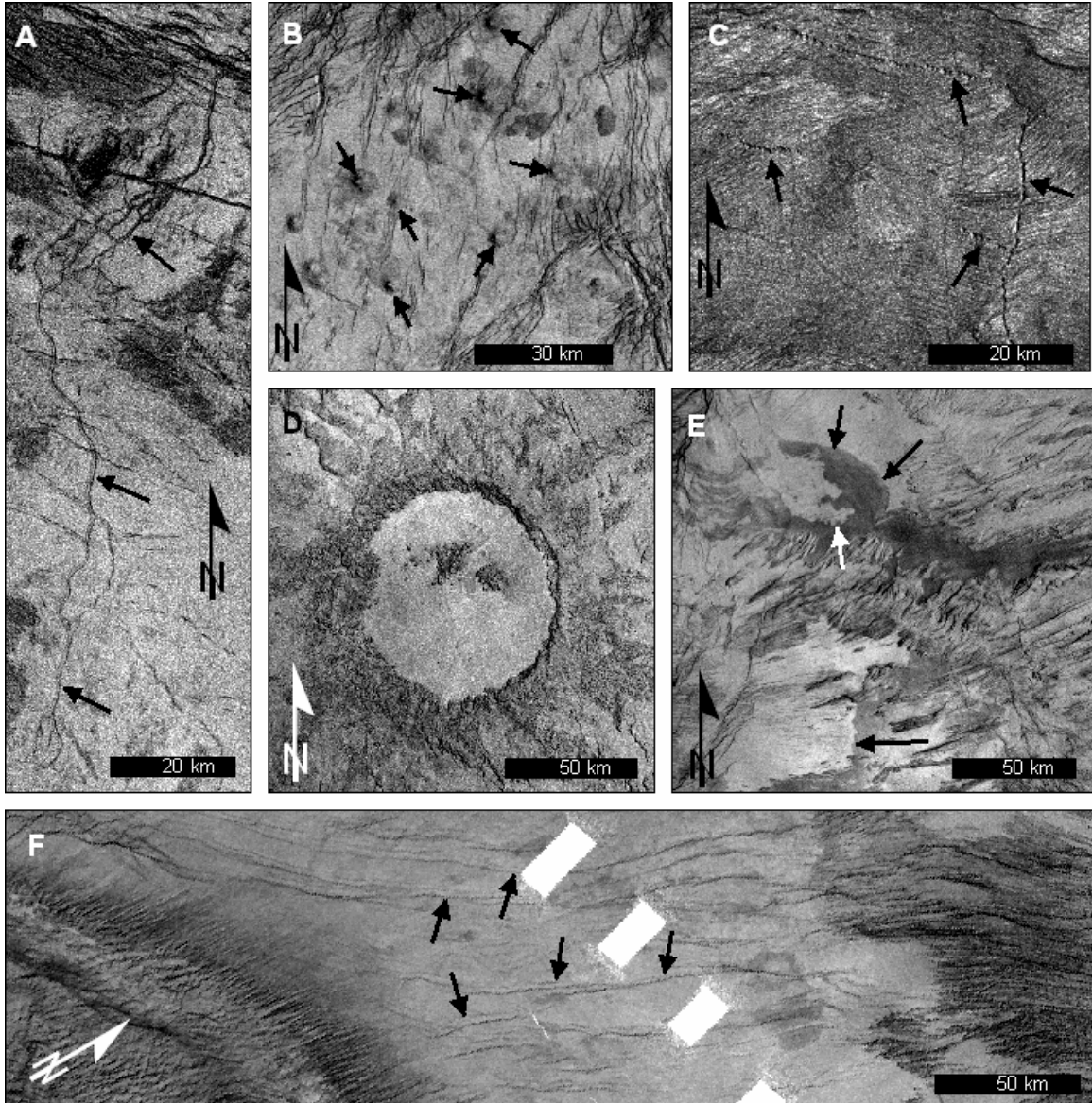


Figure 11. Examples of primary structures in V-48. A) channel, B) shields, C) pit chains, D) impact crater, E) flow fronts, F) shallow troughs. All images are left-look inverted SAR; white rectangles in F are data gaps.



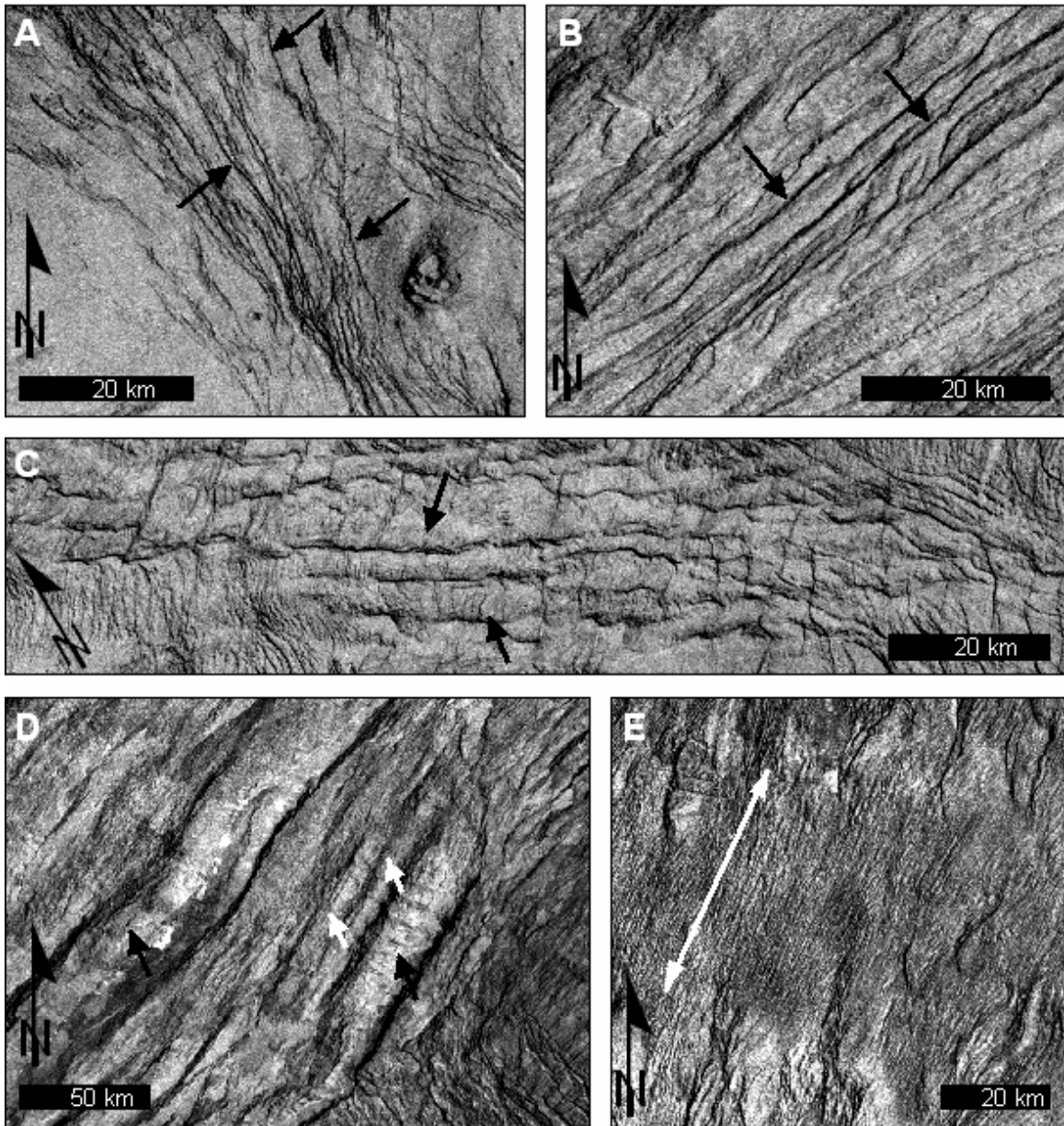


Figure 12. Examples of secondary structures mapped in V-48. A) fractures, B) lineaments, C) folds, D) ridges, black arrows point to large ridges, white arrows point to small ridges, E) penetrative fabric, with white line parallel to the trend. All images are inverted left-look SAR.

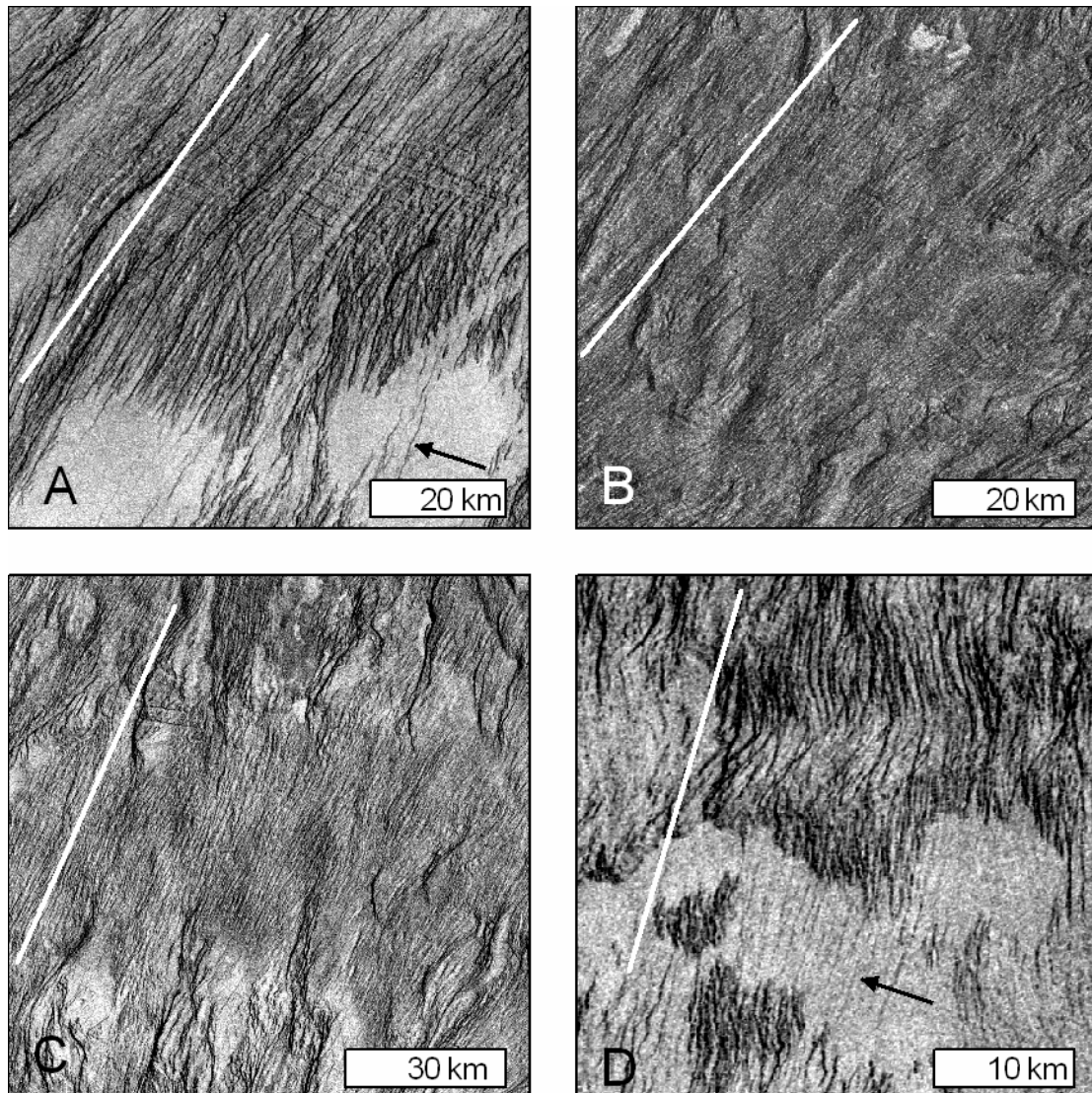
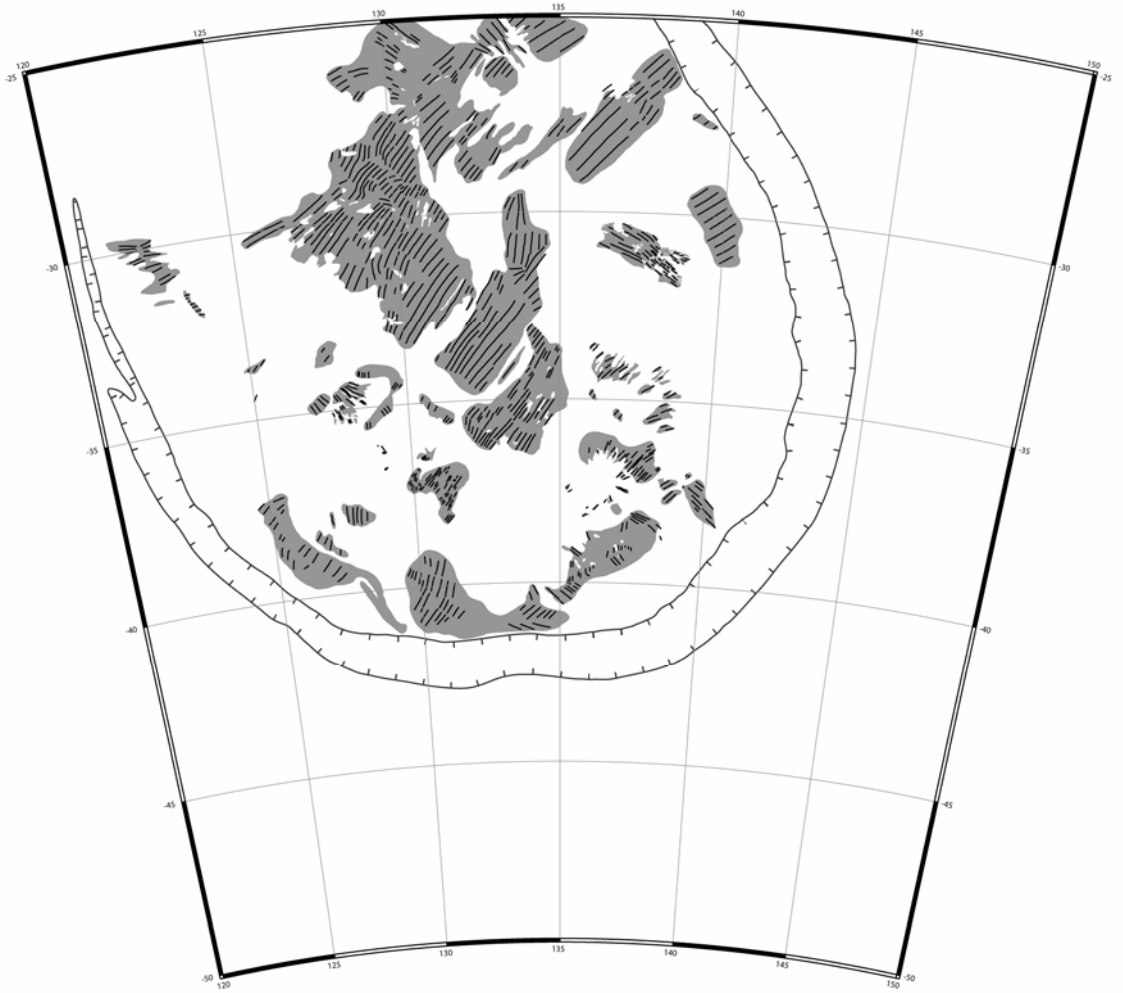


Figure 13. Representative inverted left-look SAR images of the penetrative fabric. White lines indicate fabric trends. Penetrative fabric appears fracture-like in A and D, however more commonly the fabric appears fold-like (B and C). Note the delicate interfingering of radar-smooth (low-backscatter) material into penetrative fabric lineaments (A and B), implying that cover material forms a thin layer and had a low-viscosity at time of emplacement. Black arrows indicate lineaments with the same trend as the penetrative fabric and likely represent reactivation of buried penetrative fabric structures.



**Figure 14. Map indicating location (gray fields) and trend (black lines) of penetrative fabric in the interior of Artemis. Artemis Chasma outline shown for reference.**

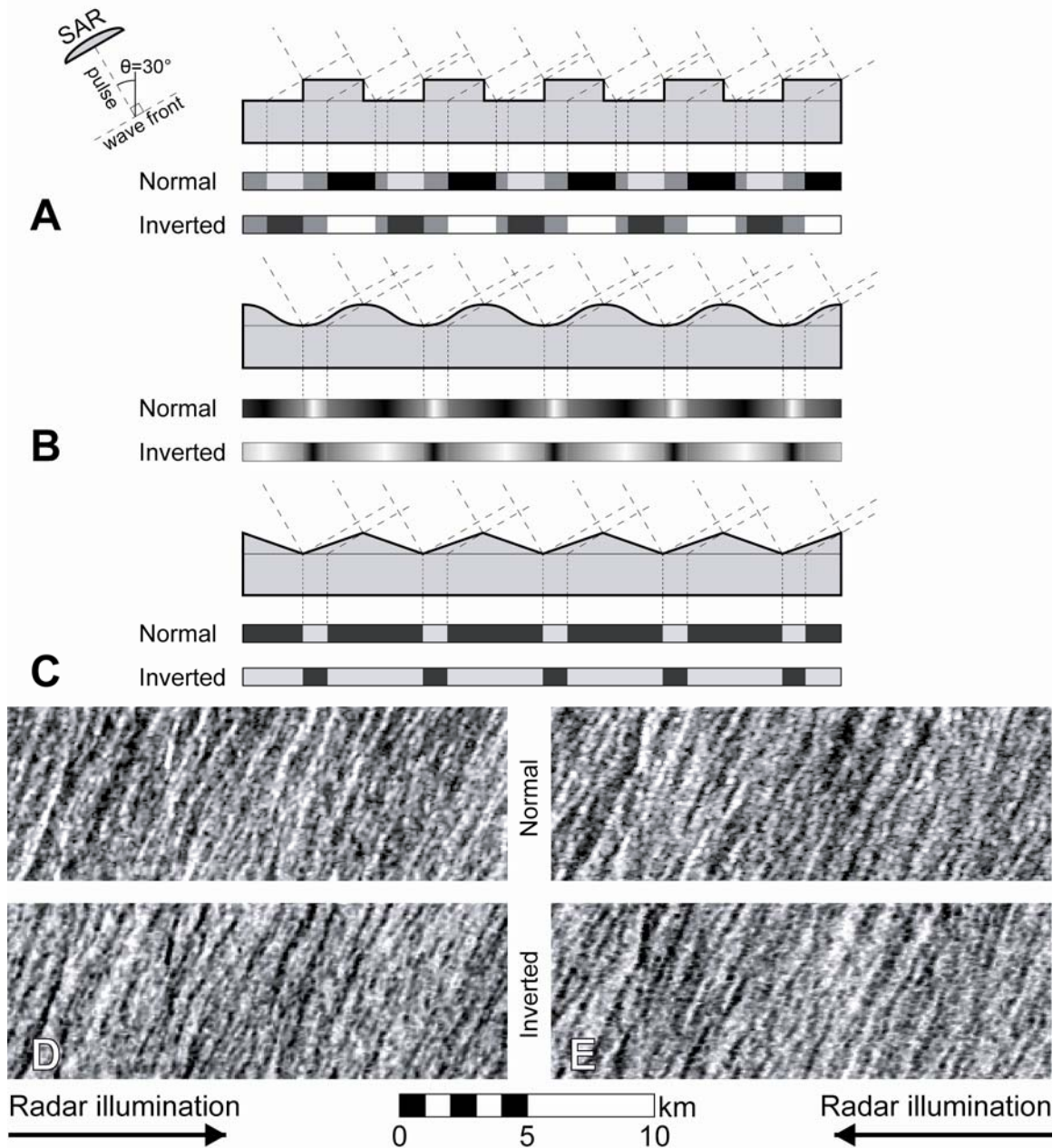
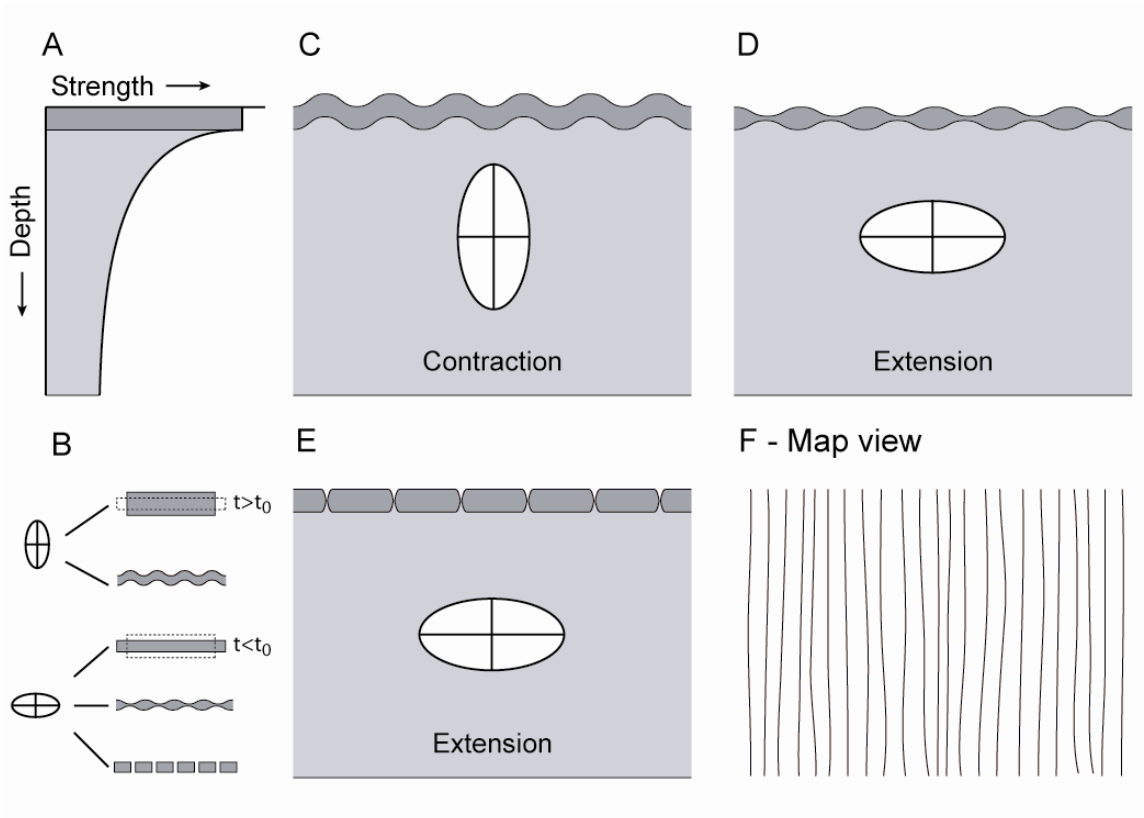
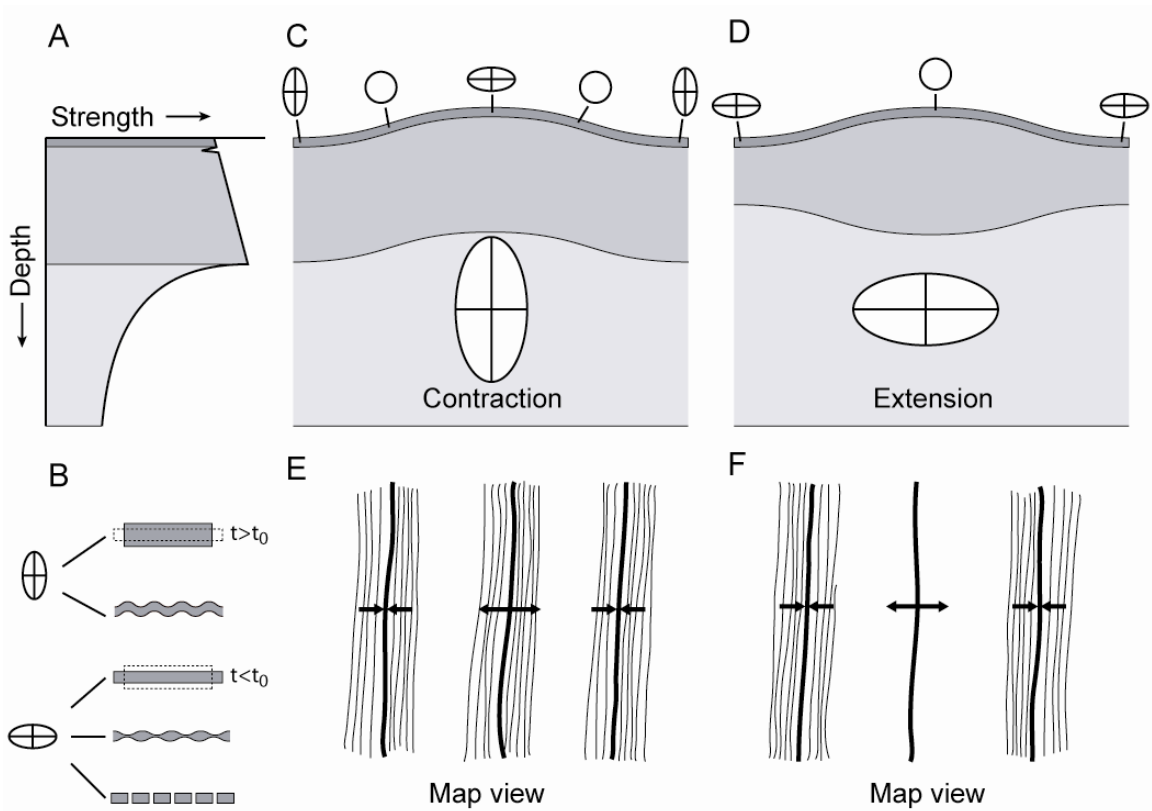


Figure 15. Various symmetric topographic shapes with the same periodicity and their predicted radar image pattern. Observations of Artemis' penetrative fabric from left-looking SAR (D,  $\theta \approx 30^\circ$ ) and right-looking SAR (E,  $\theta \approx 25^\circ$ ) most closely resemble symmetric low-amplitude rounded ridges (B).





**Figure 16. First layered thought experiment. A) Model strength profile. B) Possible deformation for bulk contraction and bulk extension. C) Contraction resulting in ductile folds at the surface. D) Extension resulting in ductile pinch and swell structures. E) Extension resulting in brittle failure. White strain ellipses indicate orientation of bulk strain only, not magnitude. F) Map view illustrates resulting pattern of structural lineaments might look the same for all three results (C-E).**



**Figure 17. Second layered tough experiment. A) Model strength profile. B) Possible deformation depending on contraction or extension in the surface layer. C) Bulk contraction results in formation of long-wavelength folds which could in turn influence the strain regime of the surface layer. D) Bulk extension results in the formation of long-wavelength pinch and swell structures which could in turn influence the strain regime of the surface layer. Map views (E and F) illustrate resulting patterns of structural lineaments corresponding to bulk contraction and bulk extension. Small strain ellipses indicate orientation of strain in the surface layer only, not magnitude. Large strain ellipses indicate orientation of bulk strain, not magnitude.**

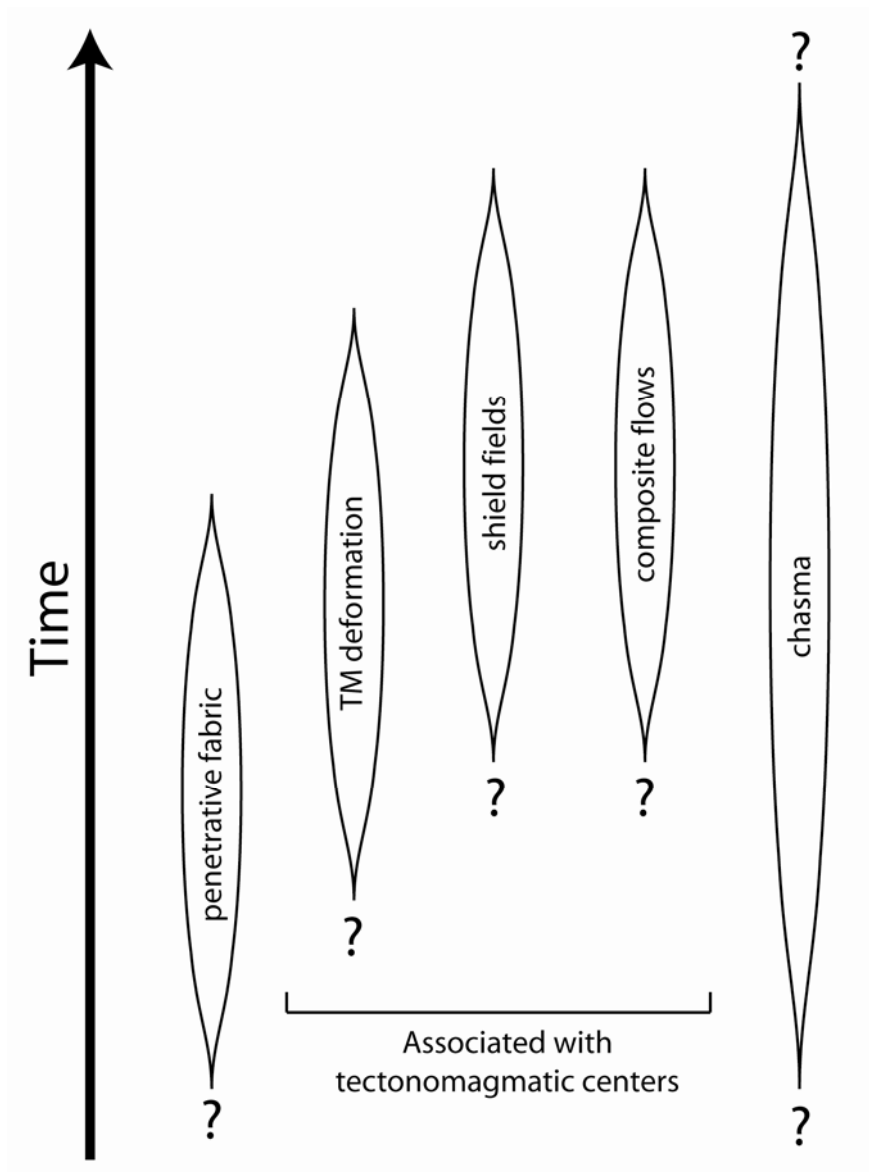
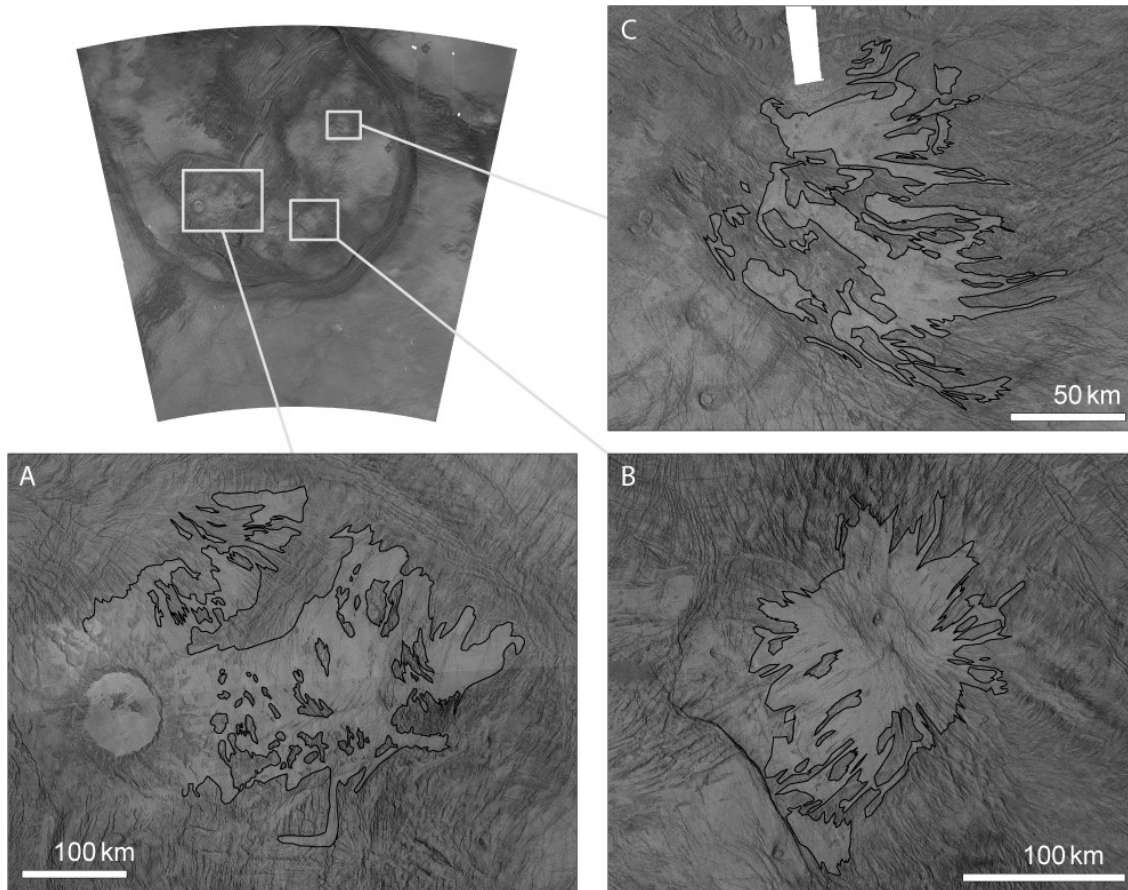
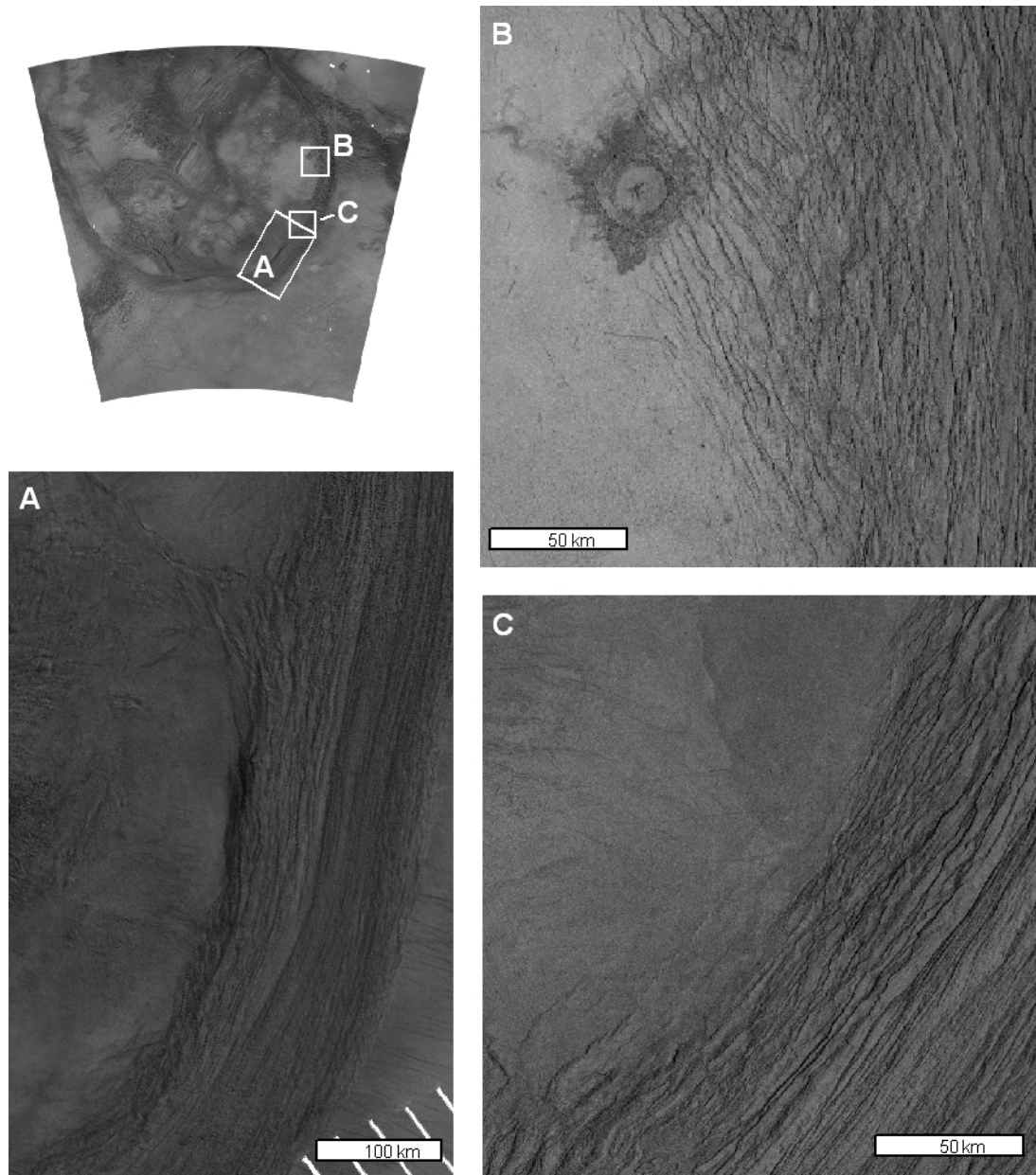


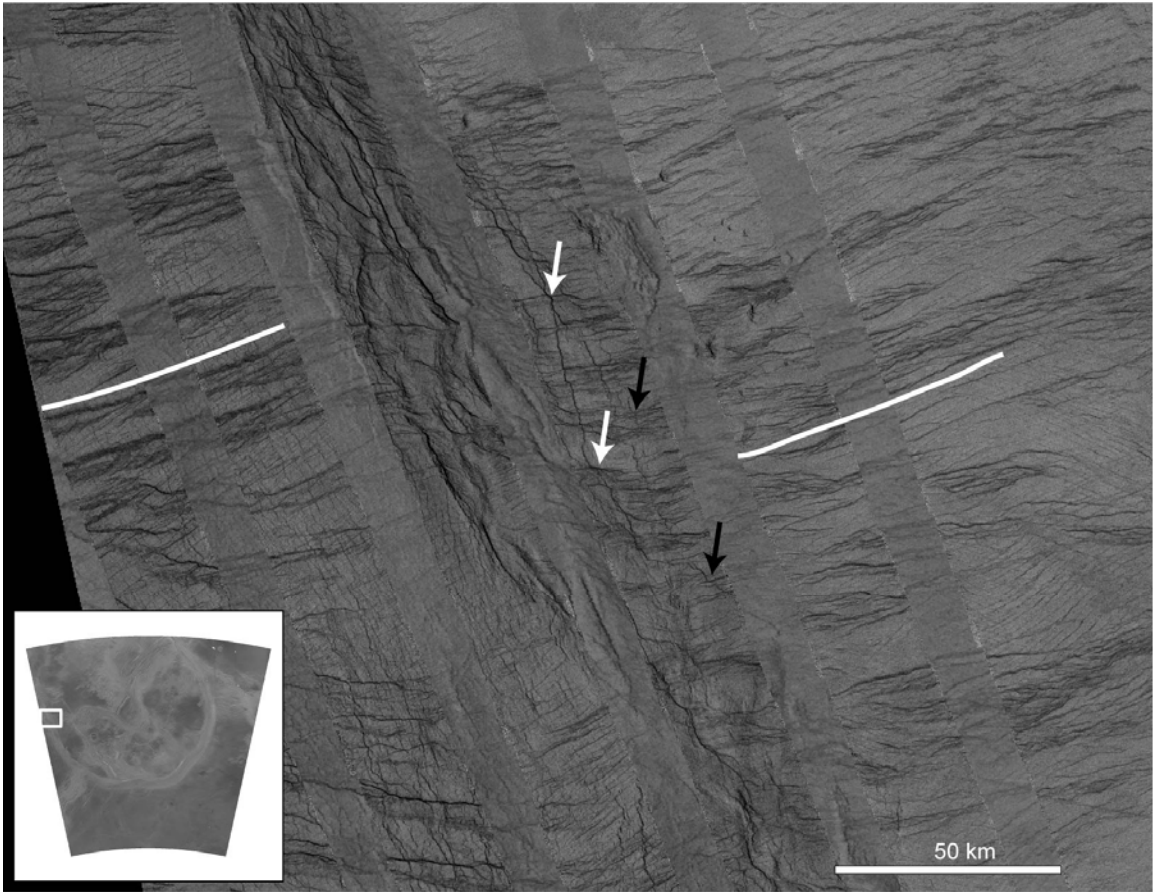
Figure 18. Relative timing of deformation and volcanism in the interior or Artemis. Queries mean the end is unconstrained. Pinching out shapes mean process gradually began or ended, otherwise width is meaningless. Length of bar does not imply duration of event.



**Figure 19. Inverted left-look SAR images of shield fields (units sfaA (A), sfbA (B), and sfcA (C)) associated with tectonomagmatic centers. Black lines delineate unit contacts. Shield fields both cover and are cut by structures related to tectonomagmatic center development.**



**Figure 20. Inverted left-look SAR images of the interaction of chasma structures with interior composite flow units. A) Chasma boundary is sharply delineated along much of the contact with unit fcbA. Chasma-parallel ridges located inward from the chasma towards the top of the image may represent reactivation of buried chasma structures. B) Chasma-parallel lineaments cut and are locally flooded by interior units. C) Chasma-parallel lineaments are locally covered by volcanic flows.**



**Figure 21. Inverted left-look SAR image of western Artemis Chasma; inset shows location. ~10 km wide diagonal stripes where radar appears discontinuous represent data-gaps in left-look SAR data filled with lower resolution right-look SAR data. White lines indicate major trend of lineaments defining shallow troughs. Arrows indicate chasma related lineaments that cut (white arrows) and are cut by (black arrows) the shallow trough lineaments.**

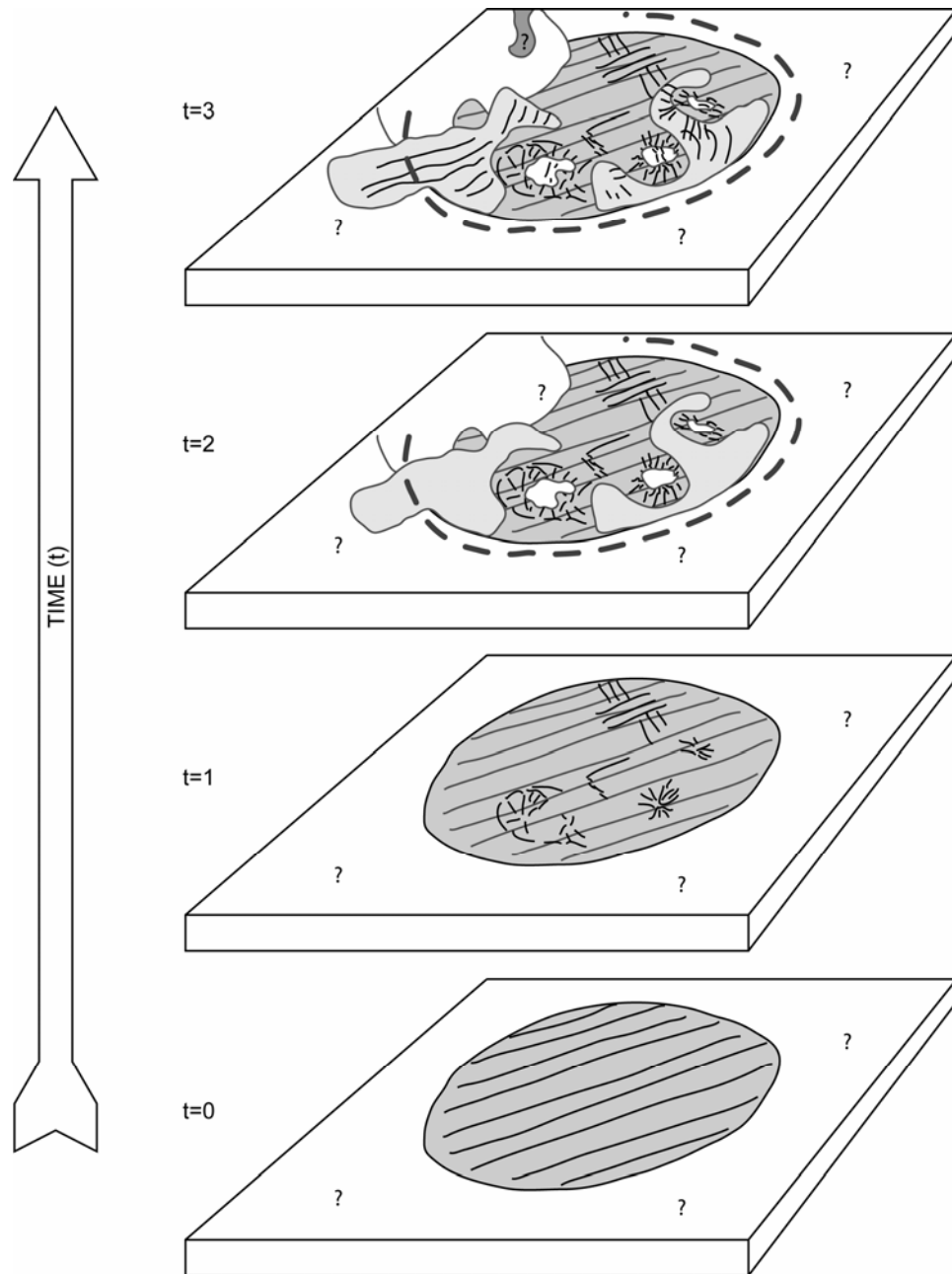


Figure 22. Cartoon block diagrams depicting the evolution of Artemis' interior region. A thin mechanically defined layer is emplaced and deformed to form penetrative fabric at  $t=0$ . Tectonomagmatic centers begin to form at  $t=1$ . Volcanic materials are emplaced during development of tectonomagmatic centers at  $t=2$ . Tectonomagmatic center development continues and deforms the relatively recent volcanic materials at  $t=3$ .


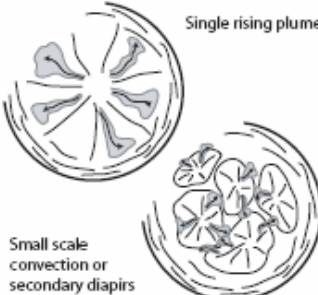
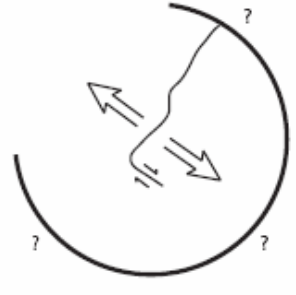










Subduction	Mantle Plume	Metamorphic Core Complex	Meteorite Impact								
											
<p>Predictions:</p> <ol style="list-style-type: none"> <li>1) interior volcanism and northwest-southeast shortening predates subduction</li> <li>2) Trough transitions from convergence to strike-slip in the northeast and southwest</li> <li>3) Southwest portion of the annulus forms prior to the northeast portion</li> <li>4) gravity anomaly over the "cold" subducting slab</li> <li>5) shallow apparent depth of compensation (i.e. in the lithosphere)</li> <li>6) normal faulting in the outer rise in response to bending of the subducting plate.</li> </ol> <p>Interior predictions:</p> <ol style="list-style-type: none"> <li>1) Volcanism predates the trough</li> <li>2) NW-SE shortening occurred first</li> </ol> <p>References: Brown and Grimm (1995, 1996), Schubert and Sandwell (1995), McKenzie et al. (1992)</p>	<p>Predictions:</p> <ol style="list-style-type: none"> <li>1) interior volcanism and deformation contemporaneous with annulus formation</li> <li>2) entire trough forms coherently and migrates either inward or outward with time</li> <li>3) gravity anomaly centered over the interior</li> <li>4) deep apparent depth of compensation (i.e. in the mantle)</li> </ol> <p>Interior predictions:</p> <ol style="list-style-type: none"> <li>1) lineaments cut and are cut by other interior lineaments and trough structures</li> <li>2) lava flows overlap in time and space</li> </ol> <p>References: Griffiths and Campbell (1991), Hansen (2002), Smrekar and Stofan (1997)</p>	<p>Predictions:</p> <ol style="list-style-type: none"> <li>1) ~170 km northwest-southeast directed extension in the center exposes deep crustal and possibly mantle rocks</li> <li>2) extension in center due to rising plume tail</li> </ol> <p>Interior predictions:</p> <ol style="list-style-type: none"> <li>1) Minimum of ~170 km NW-SE extension</li> <li>2) Extensive shear zones trending NW-SE</li> <li>3) Upper plate boundary and presence of klippe</li> </ol> <p>References: Spencer (2001)</p>	<p>Predictions:</p> <ol style="list-style-type: none"> <li>1) any preexisting deformation in the interior was obliterated by impact, i.e. interior deformation cannot predate trough formation.</li> <li>2) Artemis formed prior to 3.9 Ga</li> <li>3) Trough and paired rises may represent multi-ringed impact structure</li> </ol> <p>Interior predictions:</p> <ol style="list-style-type: none"> <li>1) All structures formed nearly instantaneously</li> <li>2) Central peak or peak ring usually associated with large impact craters</li> <li>3) Ringed margin</li> </ol> <p>References: Hamilton (2004)</p> <table border="1" data-bbox="1501 1047 1722 1266"> <thead> <tr> <th colspan="2">Explanation:</th> </tr> </thead> <tbody> <tr> <td></td> <td>trough outline</td> </tr> <tr> <td></td> <td>lineament</td> </tr> <tr> <td></td> <td>lava flow</td> </tr> </tbody> </table>	Explanation:			trough outline		lineament		lava flow
Explanation:											
	trough outline										
	lineament										
	lava flow										

Figure 23. Summary of hypotheses for Artemis' formation.



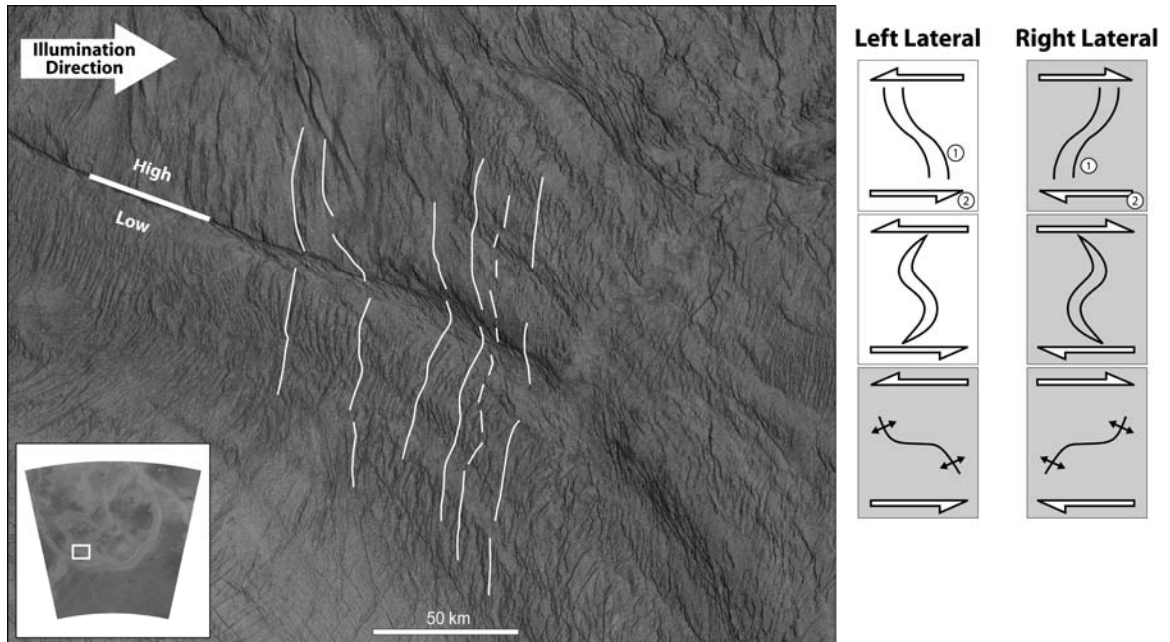


Figure 24. Inverted left-look SAR image of the southwest margin of tectonomagmatic center TMA; inset indicates location. White lines highlight lineaments that appear to change trend as they cross a ridge. Deflection may be explained solely by radar image artifacts. Cartoons at right illustrate predicted patterns of lineaments for left- and right-lateral simple shear deformation of preexisting lineaments (top), extensional structures coincident with shear (middle), and contractional structures coincident with shear (bottom). Gray boxes indicate geometries that are inconsistent with lineament trends.

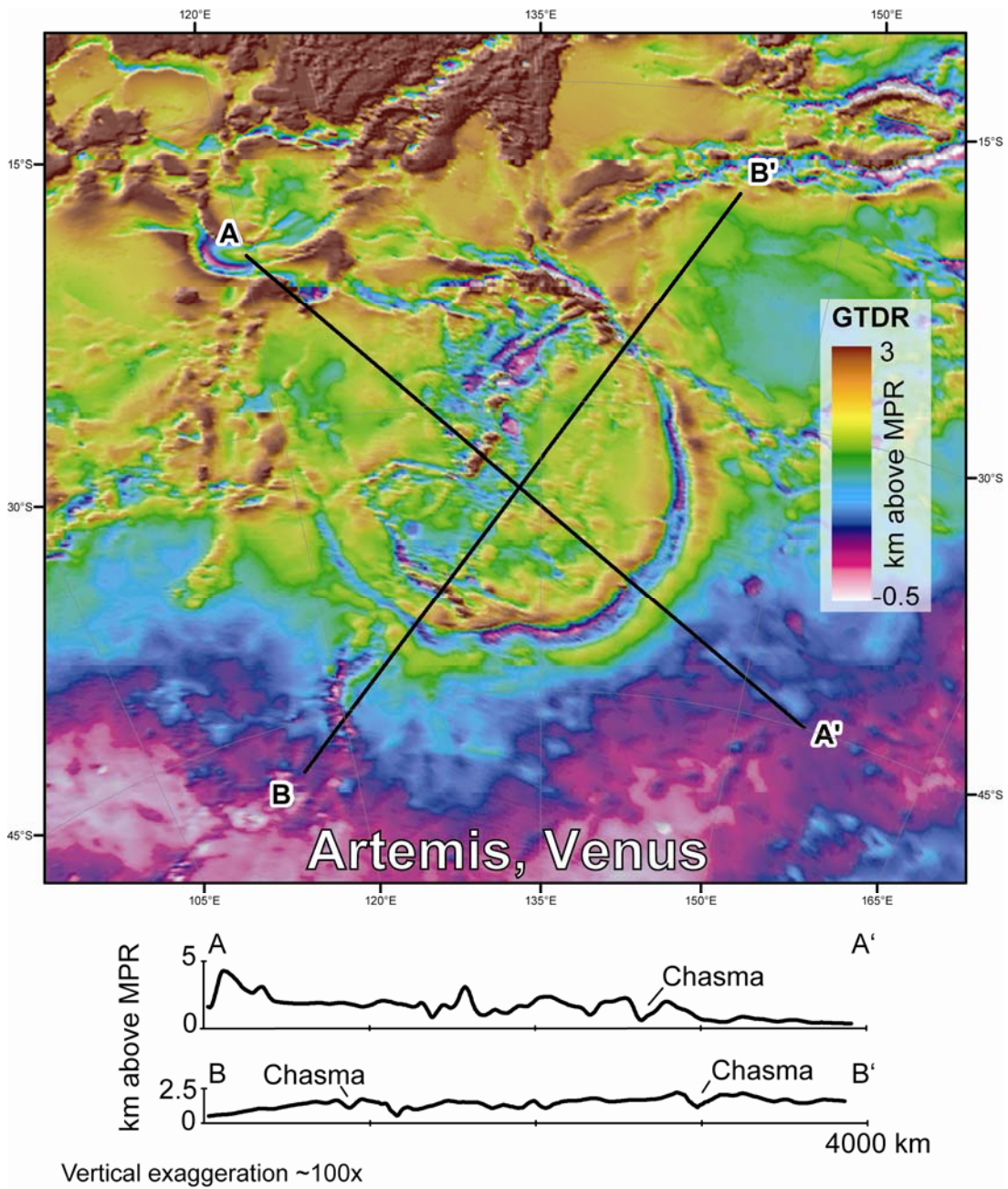


Figure 25. Topographic profiles across Artemis. Figure at same scale as Hellas Planitia topography for comparison.

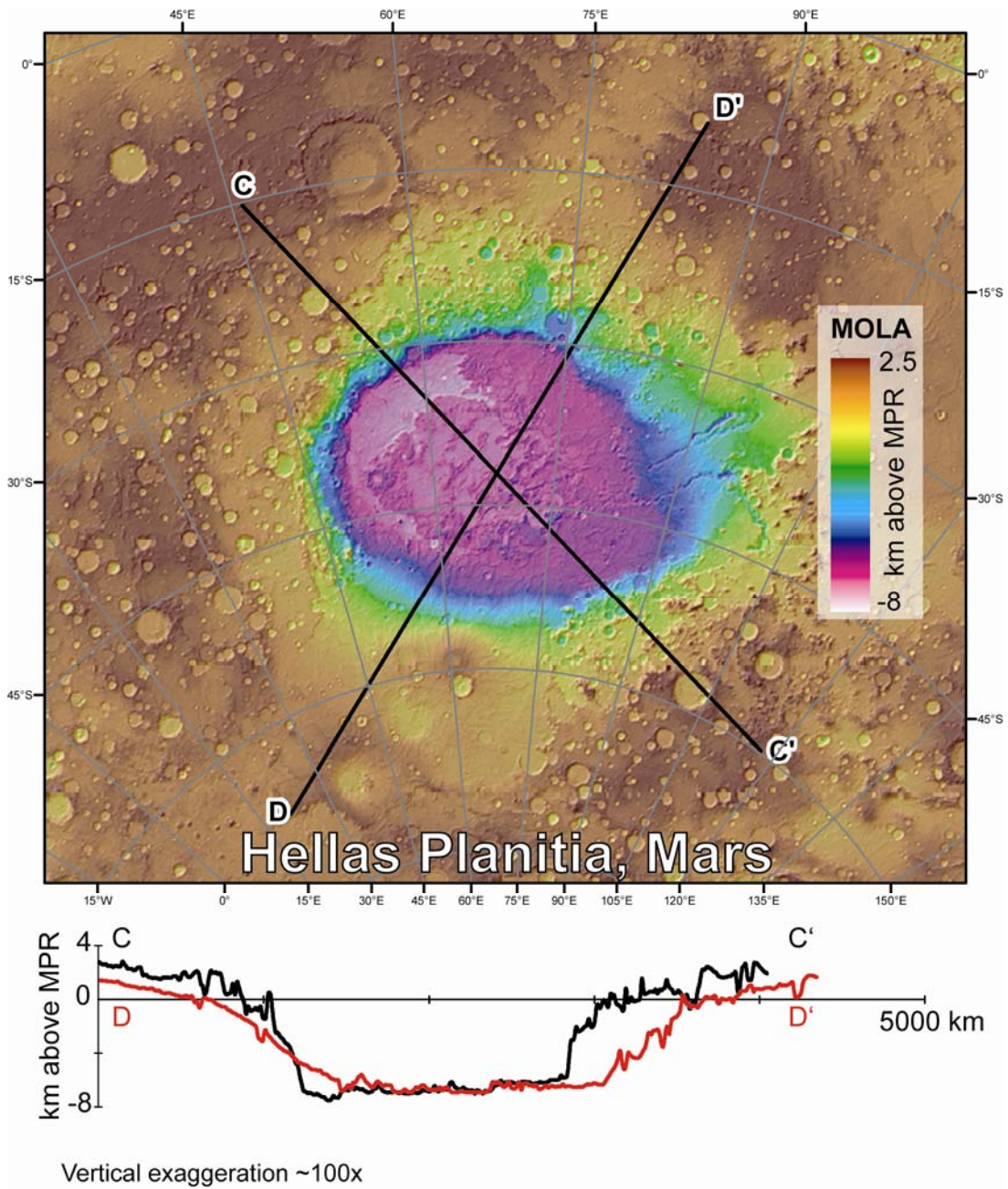


Figure 26. Topographic profiles across Hellas Planitia. Figure at same scale as Artemis topography for comparison.